PHYSICAL REVIEW FLUIDS **10**, 054604 (2025)

Structural uncertainty assessment for fire-engulfed objects in crosswind: Establishing credibility for a multiphysics wall-modeled large-eddy simulation paradigm

Stefan P. Domino [*]
Computational Thermal/Fluids Department, Sandia National Laboratories, Albuquerque, New Mexico 87109, USA and Institute for Computational and Mathematical Engineering, 475 Via Ortega, Stanford, California 94305, USA

Sarah Scott
Thermal/Fluid Science and Engineering Department, Sandia National Laboratories, Livermore, California 94551, USA

Josh Hubbard
Energetics, MultiPhase and Soft Material R&D Department, Albuquerque, New Mexico 87109, USA

(Received 20 February 2025; accepted 8 April 2025; published 7 May 2025)

A structural uncertainty validation study for a large-scale, fire-engulfed, elevated object subjected to crosswind is presented to establish the credibility of a high-fidelity, low-Mach, turbulent reacting flow wall-modeled large-eddy simulation (WMLES) approach that includes multiphysics coupling to participating media radiation and conjugate heat transfer. To establish that WMLES can accurately predict surface quantities including drag and pressure coefficient in the low-Mach crosswind regime, a foundational elevated isothermal cylinder validation case is presented at a similar gap-to-diameter ratio of 0.25, spanning the subcritical to supercritical drag regime ($\mathrm{Re}_D = 1.1 \times 10^5$ and 4.3×10^5, respectively). This study exercised both static and dynamic coefficient LES (Smagorinsky and k_{sgs}) with both local and exchange-based velocity sampling. Results showcase that the drag crisis (or the sudden drop in drag coefficient at increased Re_D) is well captured when using an exchange-based dynamic coefficient WMLES methodology, while noting lack of mesh convergence and overall drag and pressure coefficient predictively when using a static coefficient, local velocity sampling WMLES. For the $\mathcal{O}(10)$ m JP-8 liquid pool fire crosswind validation study presented, two experimental crosswind configurations (2 m/s and 9.5 m/s) are showcased for a fire-engulfed mock fuselage roughly 4 m in diameter. Using the best model-form practices identified in the isothermal study, dynamic coefficient k_{sgs} exchange-based WMLES fire validation findings demonstrate accurate peak irradiation and skin temperature predictions as a function of crosswind magnitude. Excessive yaw in the low-crosswind fuselage configuration, consistent with experimental findings, captured a significant predicted asymmetry in flame attachment and heat flux toward the downwind cylindrical cap—indicative of axial vortex structures transporting the flame along the upper and lower fuselage leeward surface. All fire mesh resolution simulations captured the experimental finding that as crosswind increased, predicted flame shape and peak irradiation magnitude onto the fuselage transitioned from a windward to a leeward cylinder location due to the migration of the upper- to lower-shear fuel/air mixing

[*]Contact author: spdomin@sandia.gov

layer thereby demonstrating the novelty, significance, and credibility of this high-fidelity WMLES reacting flow framework.

DOI: 10.1103/PhysRevFluids.10.054604

I. INTRODUCTION

Large-scale pool fires can arise during transportation accidents where hydrocarbon liquid-based fuels are used to power vehicles such as trucks and airplanes. Understanding the behavior of fire accident scenarios that include large liquid fuel inventory breaches has driven the United States Department of Energy, over the past 30 years, to invest in fire physics elucidation efforts and in the creation of high quality experimental validation data sets, cf [1–4]. Modeling and simulation development and deployment of predictive methods closely followed, starting with a Reynolds-averaged Navier-Stokes (RANS) approach for buoyant and fire-based flows [5,6] that was recently fully transitioned to a modern large-eddy simulation (LES) paradigm [7–9].

Fire accident scenarios can be defined (or parametrized), by a minimum, through the specification of the following: (1) fuel type, (2) fuel inventory size/shape, (3) the presence of crosswind, and (4) the presence of bluff bodies, i.e., objects such as trailers and airplane fuselages. Generally, the fuel type and fuel inventory levels are known based on the transportation mechanism. Ideally, to establish credibility of the mathematical modeling paradigm (here credibility is defined as the ability for an end user to trust simulation results either during a design cycle or qualification-like workflow) each of these four environmental specifications are ideally addressed within a verification and validation (V&V) set of investigations that captures uncertainty quantification (UQ). In this context, UQ can be driven from environmental factors, e.g., varying crosswind magnitude, object placement relative to the incoming wind profile, etc., or the underlying mathematical modeling approach pursued. A strong component of the mathematical modeling approach will include the effect that the numerical formulation (and mesh resolution) has on quantity of interest(s) (QoIs) along with a structural uncertainty, or sensitivity to the end QoIs that are a function of the math-model activated. For instance, math model variations may include the form of the turbulence model, combustion approach, the multiphysics participating media radiation (PMR) coupling strategy, and the presence of other multiphysics couplings such as conjugate heat transfer (CHT). In some combined use cases, a structural response to the imposed fire load is desired. Toward the quantification of sensitivities that arise due to mesh resolution effects, we reference our past efforts where the effect of mesh refinement and numerical operators for the fire application space have been captured [7–9]—a practice that is often times skipped, at the peril of the computational scientist [10].

In the fire application space, the common set of engineering QoIs generally include flame shape, fire dynamics, spatiotemporal gas phase temperature signatures, and surface quantities such as radiative and convective flux, incoming radiation, or irradiation, and thermal response. Common questions that need to be asked and answered in the context of a detailed verification and validation uncertainty quantification (VVUQ) study include the investigation of the above four environmental specifications in addition to the following mathematical set of questions: *How do QoIs vary as a function of mesh resolution? What type of numerical operators—including advection stabilization and time integration—are required for accurate results? What fidelity of math models are required to meet a given use case where the consequence of a poor simulation result may be low or high? What are the computational resources and timescales associated with providing an answer?*

The goal of establishing trust in a large-eddy simulation mathematical modeling paradigm for the fire use case first concentrated on a establishing a predictive multiphysics, unsteady flamelet-based, turbulent reacting flow simulation strategy for quiescent pool fire configurations [7]. Other LES-based approaches in the quiescent regime exist, where a suite of LES and combustion models can be exercised. For instance, in Ref. [11], LES with a Smagorinsky turbulence model was used to simulate buoyant flows. Here, a helium plume was simulated, followed by a Lagrangian thermal element combustion model that added to model a pool fire. In Ref. [12], LES with a Smagorinsky turbulence model and a probability density function (PDF) method based on the Eulerian stochastic fields method and accelerated with chemistry coordinate mapping was used for the combustion model. The one-equation k_{sgs}, Smagorinsky, and Wall-Adapting Local Eddy-viscosity turbulence models, along with different time discretization methods were evaluated for a pool fire using eddy dissipation concept (EDC) combustion model in Ref. [13]. This study found that the Smagorinsky turbulence model, which is algebraic, found "significant error with the experimental results."

The exploration of pool shape effects of like surface area have on flame structure and radiative flux at various crosswind magnitudes (ranging from 0 m/s to peak values of 20 m/s) was explored in Scott and Domino [8]. Due to boundary layer resolution expense required for crosswind fire applications, wall-modeled large-eddy simulation (WMLES) is required. Using a WMLES paradigm, classic jet-in-crossflow coherent structures including horseshoe vortices, jet shear-layer structures that arise from baroclinic torque (misaligned pressure and density gradients), column vortices, and counterrotating vortex pairs were successfully captured and linked to pool shapes of circles, squares, and high-aspect ratio rectangles. Scott and Domino also computationally established the correlation between crosswind magnitude and heat flux. Specifically, that as crosswind increased, so did predicted surface heat flux, while noting the genesis of new fine-scale flow features as the mesh resolution was increased. In all of these studies, we stress that our end use case of interest generally is defined by large pools, i.e., roughly 10 m in characteristic length and greater, and involves crosswinds ranging from quiescent, i.e., 0 m/s, to peak values of 20 m/s.

Capturing the effect that an incoming turbulent boundary layer has on flame dynamics, flame shape (including flame lengths, heights, and flame drag), and the modification of the burst/sweep cycle was presented in the WMLES study of Ref. [9] using a slightly modified model suite of Ref. [7] where a mass injection pool boundary condition was exercised (we note the full mathematical modeling suite will be overviewed in Sec. II and in the fire modeling parameter Sec. IV B). Overall, the role to which mesh resolution affects predicted QoIs such a convective and radiative heat flux, flame dynamics such as fire puffing and shedding events, and fire size were captured in our most recent works [7–9,14]. Across the field, these QoIs have been examined by many researchers, however the interaction between mesh resolution and QoIs is lacking. The transition to turbulence for pool fires, including puffing and core collapse, for laboratory scale fires (25 cm and lower diameters) was examined in Ref. [15], where an automatic mesh refinement strategy was used. We find such methods extremely powerful, while noting increased application complexity in the generalized unstructured regime, along with a required algorithmic advancement for error indicators that accurately determine refinement and de-refinement zones. In Ref. [16], the radiation feedback to the pool surface was researched in a small-scale pool fire, but only a single mesh resolution is presented. Similarly, in Ref. [17] turbulence-radiation interaction effects in LES of medium scale pool fires was assessed, but again for a single where mesh convergence was not addressed.

The presence of bluff body interactions and how QoIs are affected represents the most commonly requested engineering question to be answered, and within a simulation study, whether or not the underlying mathematical modeling approach can capture key fire features. For example, in the seminal outdoor experimental study of Suo-Antilla and Gritzo [3], which forms the basis experimental data set provided in this paper, the importance of convective heat transfer, flame impingement, and attachment was investigated. Experimental findings showcased the strong sensitivity of flame shape attachment to a large-scale mock fuselage (roughly 4 m in diameter) exposed to an $\mathcal{O}(10)$ m and $\mathcal{O}(20)$ m pool fire as a function of crosswind magnitude. In Refs. [18,19], the evaluation of the effects that crosswind has on fire was investigated using the well-controlled facility at Sandia National Laboratories and exercised a hybrid RANS approach [5] where the concept of temporal filtering was established. In Ref. [20], a LES simulation of a fire with obstacles in an engine room was conducted. Here they found that the of the size and height of the cylindrical obstacle determined the effect on the fire plume. Finally, in Ref. [21] the thermal response of a series of objects engulfed in a 7.9 m JP-8 pool fire was evaluated using WMLES to asses the EDC and unsteady flamelet turbulent combustion models. This study found that both combustion models were effective in predicting QoIs such as convective and radiative heat flux to a series of engulfed cylindrical objects.

Outside of Sandia, researchers have studied the interaction between pool fires and engulfed objects. Recent numerical studies for large scale fires have been studied by Ref. [22], where an aircraft crash and burn scenario was evaluated in a range of crosswinds using LES. In this work, they used the one-equation k_{sgs} approach, a discrete ordinate method [23] (DOM) for participating media radiation, and the EDC model for combustion. This research group numerically evaluated an aircraft in a 20 m pool fire under quiescent, 2, 5, and 10 m/s crosswinds. Additionally, in Ref. [24] 21.6 m^2 pool fire surface area experiments were conducted with a 1.1 by 2.4 m (length and diameter) tank fully engulfed in the fire. Along with the experiments, LES simulations in NIST's Fire Dynamics Simulator [25] were conducted. The authors found reasonable agreement in temperature on the engulfed object between the experiments and the simulations. However, the effects of simulation parameters, e.g., model choice, numerical parameters, mesh resolution, etc., to the simulation results are not presented in either of these works. Few additional studies exist of computational fluid dynamics-based investigation of objects engulfed in a pool fire, likely due to computational complexity and cost. More generally, wildland fire research has focused on understanding and predicting complex dynamics of whirls and shedding events with variations in terrain and plant matter [26], in addition to including interactions between the fire and the atmospheric boundary layer [27], where the underlying math model representation of the fire is less described.

While the above works have contributed to providing further confidence in the modeling of pool fires—in addition to increased physics-based understanding of large-scale fires with and without crosswind—inclusion of fire-engulfed objects in the presence of appreciable crosswind represents a current credibility gap. This is especially true when deploying wall-modeled LES that exercises "state-of-the-practice" wall modeling approaches such as exchange-based methods [28] where a sampled velocity field off of the wall is used, or where dynamic-coefficient LES models are activated. In fact, inclusion of objects in crosswind drive new complex flow structures, for example, when considering an airplane-based accident scenario that can encompass classic cylinder-in-crosswind physics. However, due to the proximity of the fuselage to the ground level, an elevated cylinder use case arises. The elevated cylinder use case drives clear upper and lower shear layers due to unsteady separation at the top and bottom cylinder location. Regions of increased mixing entrain fuel and air, driving increased combustion efficiency and radiative heat fluxes both to the ground and object. Preliminary studies by Domino [14], which forms the basis of this complete isothermal and fire-engulfed research effort, attempted to close the credibility gap for objects engulfed in fire exposed to both low- and high-crosswind, i.e., $\mathcal{O}(1)$ to $\mathcal{O}(10)$ m/s. Here, it was established that a static-coefficient local velocity sampling WMLES fire modeling approach could reasonably predict incoming radiative heat fluxes to the surface of complex objects, in addition to predicting the migration of flame structure from the windward to leeward fuselage location. Due to the reduced scope of this initial research effort, a dynamic coefficient LES procedure with exchange-based velocity sampling for the equilibrium model was suggested for future work—as was the deployment of a complete structural uncertainty investigation of WMLES for an isothermal, elevated cylinder-in-crosswind configuration that mimicked the fire crosswind use case. Based on our current understanding of the body of published research, an advanced WMLES approach that uses exchange-based velocity sampling has neither been evaluated for an elevated cylinder within the subcritcal-to-supercritical regime, nor exercised within the fire application regime, again showcasing the novelty and importance of our present study.

The primary goal of our paper is to execute a validation hierarchy for elevated objects subjected to crosswind—both with and without the presence of fire—that supports the ability to resolve the following a frequently posed question by safety engineers: *Can a multiphysics, low-Mach, state-of-the-art unstructured WMLES approach accurately predict windward-to-leeward migration of heat fluxes (mean and peak values) on an elevated fire-engulfed object as crosswind increases?*

For this novel yet significant credibility advancement, two validation use cases are provided: an isothermal flow past an elevated cylinder within the subcritical and supercritical drag regimes [29], and a pool fire-engulfed elevated mock fuselage in the presence of two mean crosswinds of 2.0 and 9.5 m/s [3]. Structural uncertainty quantification for WMLES is of paramount interest and included in the comprehensive study. Specifically, both static and dynamic coefficient LES (Smagorinsky and one-equation k_{sgs} model) with both local and exchange-based velocity sampling are presented for the isothermal elevated cylinder case. Section II captures the math modeling and numerical overview where details of the multiphysics turbulent reacting flow capability is described. Validation results for a turbulent, isothermal elevated cylinder configuration, which includes a comprehensive structural uncertainty exploration, are provided in Sec. III. In Sec. IV, we deploy the model-form lessons learned from the isothermal validation case to the fire-engulfed object in a crosswind validation study. Both validation sections include detailed physics, mesh, and numerical parameter descriptions. Finally, conclusions and future work are outlined in Sec. V.

II. LOW-MACH EQUATION SET

In this section, key attributes associated with the modeling of a fire-engulfed object are highlighted. Full details of the model suite and numerical implementation can be found in the Advanced Simulation and Computing Sierra/Fuego Theory Manual [30] and in Ref. [7], where the LES and combustion modeling objectives are provided. The details of the mathematical model suite begin with the integral form of the variable-density, low-Mach equation set expressed in Favre-filtered form are provided for the variable-density continuity and momentum equations,

$$\int \frac{\partial \bar{\rho}}{\partial t} \mathrm{d}V + \int \bar{\rho} \widetilde{u}_j n_j \mathrm{d}S = 0, \tag{1}$$

$$\int \frac{\partial \bar{\rho} \widetilde{u}_i}{\partial t} \mathrm{d}V + \int \bar{\rho} \widetilde{u}_i \widetilde{u}_j n_j \mathrm{d}S = \int \widetilde{\sigma}_{ij} n_j \mathrm{d}S - \int \tau_{ij}^{\mathrm{sgs}} n_j \mathrm{d}S + \int (\bar{\rho} - \rho_\circ) g_i \mathrm{d}V. \tag{2}$$

Above, $\bar{\rho}$ and $\tilde{u}_i$ are the density and velocity, respectively, while the buoyancy source term includes the reference density, $\rho_\circ$, and gravitational acceleration vector g_i. Favre-filtered variables are designated as $\tilde{\cdot}$, while volume and surface integrals are differentiated via the dV and dS usage, respectively. The stress is defined by

$$\sigma_{ij} = 2\bar{\mu} \tilde{S}_{ij}^* - \bar{P} \delta_{ij}, \tag{3}$$

and the traceless rate-of-strain tensor is defined as follows:

$$\tilde{S}_{ij}^* = \frac{1}{2}\left(\frac{\partial \tilde{u}_i}{\partial x_j} + \frac{\partial \tilde{u}_j}{\partial x_i} \right) - \frac{1}{3} \frac{\partial \tilde{u}_k}{\partial x_k} \delta_{ij}. \tag{4}$$

The subgrid scale turbulent stress τ_{ij}^{sgs} is defined as

$$\tau_{ij}^{\mathrm{sgs}} \equiv \bar{\rho} (\widetilde{u_i u_j} - \tilde{u}_i \tilde{u}_j), \tag{5}$$

and is closed via a suite of LES models. Specifically, in this research effort the algebraic Smagorinsky model [31] and the one-equation subgrid scale kinetic energy k_{sgs} model [32] are exercised—each of which has been extended to the dynamic coefficient regime [33,34]. Both models are cast within an isotropic turbulent viscosity closure paradigm where alignment between the subgrid scale stress and rate of strain is assumed, along with the supplemental relationship for the turbulent viscosity, μ_t.

For the less commonly used k_{sgs} model (here, $k_{\text{sgs}} = (\widetilde{u_k u_k} - \tilde{u}_k \tilde{u}_k)$) for completeness, the transport equation is given by

$$\int \frac{\partial \bar{\rho} k_{\text{sgs}}}{\partial t} \mathrm{d}V + \int \bar{\rho} \tilde{u}_j k_{\text{sgs}} n_j \mathrm{d}S = \int \left(\frac{\mu}{\sigma} + \frac{\mu_t}{\sigma_k} \right) \frac{\partial k_{\text{sgs}}}{\partial x_j} n_j \mathrm{d}S + \int (P_k - D_k) \mathrm{d}V. \tag{6}$$

Above, P_k is the standard production term, $P_k = \tau_{ij}^{\text{sgs}} \frac{\partial \tilde{u}_i}{\partial x_j}$, σ and σ_k are the laminar and turbulent Schmidt number (0.9 and 1.0, respectively), while the dissipation term is closed by

$$D_k = \bar{\rho} C_\epsilon \frac{k_{\text{sgs}}}{\Delta}. \tag{7}$$

For this LES model, turbulent viscosity, μ_t, closure is given by

$$\mu_t = \rho C_\mu \Delta \sqrt{k_{\text{sgs}}}. \tag{8}$$

Above, the filter Δ is closed by use of the control volume, $\Delta = V^{1/3}$, while the constants C_μ and C_ϵ can either be statically specified (0.845 and 0.0856, respectively) or dynamically computed as extensively outlined in Ref. [34].

The supplemental equation set including mixture fraction, $\widetilde{Z}$, static enthalpy $\widetilde{h}$, source enthalpy $\widetilde{h}_c$, soot moles-per-mass, $\widetilde{N}_s$, and soot mass fraction $\widetilde{Y}_s$ are as follows:

$$\begin{aligned}
&\int \frac{\partial \bar{\rho} \widetilde{Z}}{\partial t} \mathrm{d}V + \int \bar{\rho} \tilde{u}_j \widetilde{Z} n_j \mathrm{d}S = \int \left(\frac{\bar{\mu}}{\mathrm{Sc}} \frac{\partial \widetilde{Z}}{\partial x_j} - \tau_{Z,j}^{\text{sgs}} \right) n_j \mathrm{d}S + \int \dot{S}_Z \, \mathrm{d}V, \\
&\int \frac{\partial \bar{\rho} \widetilde{h}}{\partial t} \mathrm{d}V + \int \bar{\rho} \tilde{u}_j \widetilde{h} n_j \mathrm{d}S = \int \left(\frac{\bar{\mu}}{\mathrm{Pr}} \frac{\partial \widetilde{h}}{\partial x_j} - \tau_{h,j}^{\text{sgs}} \right) n_j \mathrm{d}S - \int \frac{\partial \bar{q}_j^r}{\partial x_j} \mathrm{d}V, \\
&\int \frac{\partial \bar{\rho} \widetilde{h}_c}{\partial t} \mathrm{d}V + \int \bar{\rho} \tilde{u}_j \widetilde{h}_c n_j \mathrm{d}S = \int \left(\frac{\bar{\mu}}{\mathrm{Pr}} \frac{\partial \widetilde{h}_c}{\partial x_j} - \tau_{h_c,j}^{\text{sgs}} \right) n_j \mathrm{d}S, \\
&\int \frac{\partial \bar{\rho} \widetilde{N}_s}{\partial t} \mathrm{d}V + \int \bar{\rho} \tilde{u}_j \widetilde{N}_s n_j \mathrm{d}S = \int \left(\frac{\bar{\mu}}{\mathrm{Sc}_s} \frac{\partial \widetilde{N}_s}{\partial x_j} - \tau_{N_s,j}^{\text{sgs}} \right) n_j \mathrm{d}S + \int \dot{S}_{N_s} \, \mathrm{d}V, \\
&\int \frac{\partial \bar{\rho} \widetilde{Y}_s}{\partial t} \mathrm{d}V + \int \bar{\rho} \tilde{u}_j \widetilde{Y}_s n_j \mathrm{d}S = \int \left(\frac{\bar{\mu}}{\mathrm{Sc}_s} \frac{\partial \widetilde{Y}_s}{\partial x_j} - \tau_{Y_s,j}^{\text{sgs}} \right) n_j \mathrm{d}S + \int \dot{S}_{Y_s} \, \mathrm{d}V.
\end{aligned} \tag{9}$$

Above, Pr and Sc are the Prandtl and Schmidt numbers, respectively, while the general subgrid scale turbulent diffusive flux vector for variable ϕ, $\tau_{\phi,j}^{\text{sgs}}$, is defined as

$$\tau_{\phi,j}^{\text{sgs}} \equiv \bar{\rho} (\widetilde{\phi u_j} - \tilde{\phi} \tilde{u}_j). \tag{10}$$

A gradient-diffusion closure model is used for $\tau_{\phi,j}^{\text{sgs}}$ in the context of an isotropic, eddy-viscosity large-eddy simulation closure. A detailed description of the complicated soot-based source terms can be found in Ref. [7]. Multiphysics coupling for the full fire physics, whose detail is captured in Ref. [7], uses an operator-split participating media radiation (PMR) solver, which will be described below, to obtain the divergence of radiative flux, $\bar{q}_j^r$, thus closing the gas phase coupling with the static enthalpy equation [35].

The low-Mach method used in this paper is an equal-order, pressure-stabilized, approximate pressure projection-based scheme [36] applied on generalized unstructured mesh topologies. A control-volume finite-element method (CVFEM) is used to define a dual mesh for element topologies that include hexahedral, tetrahedral, pyramid, and wedge elements. Time advancement is achieved using a three state, second-order implicit BDF2 time integrator. For more information on the underlying unstructured discretization and the suitability of this approach for LES, see

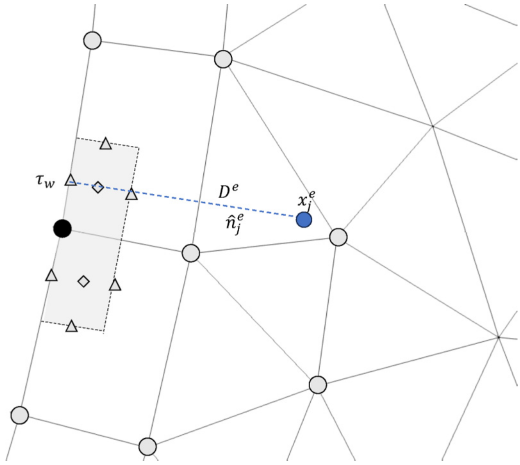

FIG. 1. Exchange-based CVFEM wall function overview where the wall shear stress, τ_w, is computed using the velocity sampled at exchange point, x_j^e. Shown in this image is the dual control volume (shaded region) with surface and volume integration points (triangles and diamonds, respectively). In this formulation, the user specifies the wall-normal distance, D^e, whose unit normal, $\hat{n}_j^e$, is formed by the boundary integration area vector. This distance can be kept constant while the mesh is refined, as is done in this paper, or modified as a function of refinement. In the limit of zero wall-normal distance, the method reverts to Fuego's default "local" velocity sampling. For nonisothermal flows, the sampled exchange point also includes a temperature reconstruction.

Refs. [37,38], while for details of the stabilization approach and low-Mach unstructured numerical overview can be found in Ref. [39].

For wall modeling, an equilibrium approach is followed, where the sampled velocity is either the near-wall, i.e., local control volume value, or at an offset exchange location [28] whose value is obtained by an unstructured parallel search. For graphical depiction of the CVFEM exchange-based velocity sampling, the reader is referred to Fig. 1. For nonisothermal effects, the equilibrium model is modified by the so-called P-function [40]. At present, no laminar-to-turbulent transition model is activated, although we expect that as Reynolds number increases, or where increased inlet turbulence intensity is found [41], we anticipate this model may perform better. For details on the static/dynamic Smagorinsky and one-equation subgrid kinetic energy k_{sgs} implementation, see Ref. [30].

The combustion model deployed in this study exercises an unsteady flamelet reacting flow procedure that allows for generalized heat loss that can occur to the surrounding environment through the presence of walls and general participating media radiation. In this approach, the thermochemical state is provided via a preprocessed multidimensional table [7] and is principled via a separation of the numerical evolution of the turbulent flow field from the chemistry through the introduction of a conserved mixture fraction, $\widetilde{Z}$, that represents a local mass fraction originating from the fuel stream. To allow for subgrid fluctuation effects that contribute to property evaluation and source terms, a presumed probability density function is used [42]. As part of a preprocessing step, a suite of adiabatic flamelets are evolved using an unsteady flamelet methodology whose underlying flamelet equation includes a generic heat loss term. Scalar dissipation rate is also varied over the range of physical values found in fires, i.e., ranging from 10^{-3} s^{-1} to larger timescale that correspond to extinction timescales (50 s^{-1}) [7] and is algebraically closed; see Ref. [30]. Each flamelet, which is based on a specific heat loss/gain and scalar dissipation rate, are saved to a multidimensional table that is used during the turbulent reacting fluids solve to provide properties such as density, viscosity, and specific heat. The four-dimensional flamelet library includes model inputs of mixture fraction, mixture fraction variance, scalar dissipation, and heat loss. We again model the hydrocarbon pool fire as a liquid heptane fuel and activate the Aksit and Moss soot model [43] that includes the effect of nucleation, coagulation, surface growth, and oxidation, as exercised in Refs. [7,9]. For complete details on the underlying combustion and soot models the reader is again referred to Ref. [7].

The method of discrete ordinates [23] is used to solve the radiative transport equation system (code name "PMR," owing its numerical roots to the open-source low-Mach code, Nalu [35]). The symmetric quadrature set of Thurgood [44] is used for the quadrature set order, N. Use of the Thurgood quadrature results in $8N^2$ ordinate directions solved during each RTE iteration. Thus, the discrete set of RTE solved for each ordinate, k, is as follows:

$$s_i^k \frac{\partial}{\partial x_i} I^k + \overline{\alpha} I^k = \overline{I}_b = \frac{\overline{\alpha \sigma T^4}}{\pi}, \tag{11}$$

where $\overline{\alpha}$ is the absorption coefficient, I^k is the intensity along the direction s_i^k, and T is the temperature. The black body radiation is designated as $\overline{I}_b$ where it is stressed that this source term includes turbulence radiation interaction effects and is provided via a table look-up. The set of radiative transport equation reduces to a set of linear, decoupled equations for each intensity when scattering is neglected, and for configurations that include nonreflecting boundaries. The intensity boundary condition assumes a diffuse, gray surface,

$$I(s) = \frac{1}{\pi}\big(\tau \sigma T_\infty^4 + \epsilon \sigma T_w^4 + (1 - \epsilon - \tau) H\big), \tag{12}$$

where τ and ϵ are the transmissivity and emissivity, respectively, while the background reference temperature and surface wall temperature are T_∞ and T_w, respectively. Finally, H is the irradiation, or sum of incoming intensities to the surface (in this paper, we use the term irradiation interchangeably with "incoming radiative flux"). Next, the divergence of radiative flux is obtained from the DOM solver and forms a linearized right-hand-side source term for the static enthalpy equation,

$$\frac{\partial \bar{q}_j^r}{\partial x_j} = \alpha(4\sigma \bar{T}^4 - G), \tag{13}$$

where G is the scalar flux, or $G = \sum_k w_k I^k$ (here, w_k are the weights provided by the Thurgood quadrature set). Details of the turbulence radiative interaction closure, which uses the presumed PDF flamelet modeling approach, can be found in Ref. [7].

Finally, the surface boundary condition for the thermal heat conduction solve due to irradiation and generalized conjugate heat transfer coupling with the fluid, is given by

$$-\lambda \frac{\partial T}{\partial x_j} n_j dS = \epsilon(\sigma T^4 - H) dS, \tag{14}$$

and

$$-\lambda \frac{\partial T}{\partial x_j} n_j dS = h(T - T^o) dS, \tag{15}$$

where λ is the thermal conductivity, ϵ is the surface emissivity, and σ is the Stefan-Boltzman constant. The heat transfer coefficient and reference temperature, h and T^o are obtained by the fluid surface transfer with the surface temperature managed by the thermal solve. For complete details associated with the thermal code Aria, see Ref. [45]. For more background on the coupling approach, which includes multiphysics code verification, the reader is referred to Refs. [7,46], while in Fig. 2, a graphical representation of the coupling is depicted.

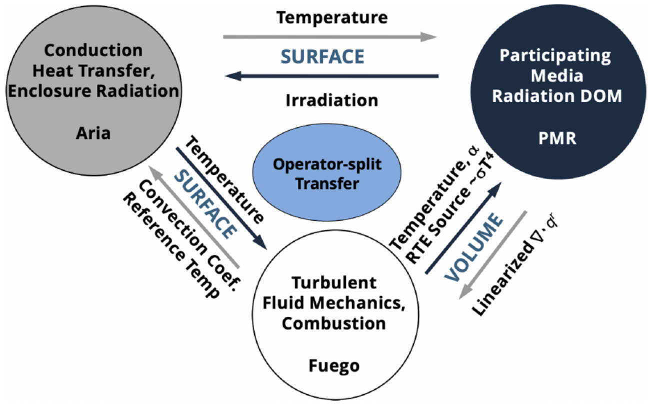

FIG. 2. Graphical depiction of the fluids, PMR, and thermal region coupling strategy that captures both surface and volume geometric transfers thus supporting nonconfomal meshing per physics region.

III. ELEVATED CYLINDER IN CROSSWIND VALIDATION: $\mathrm{Re}_D = 1.1 \times 10^5$ AND 4.3×10^5

In the experimental configuration of Ref. [29], a 0.196 m diameter (D) cylinder was situated above a wall, providing a gap (G) range of $0 \leqslant G/D \leqslant 1$ for a variety of Reynolds numbers spanning the classic cylindrical subcritical-to-supercritical drag crises regime, i.e., $1.1 \times 10^5 \leqslant \mathrm{Re}_D \leqslant 4.3 \times 10^5$. Here the gap is specifically defined as the distance between the lower cylindrical surface, i.e., $\theta = 270^\circ$, and the ground location. The experiment measured integrated drag (C_D) and lift (C_L) coefficients, in addition to pressure coefficient (C_p) at 16 angles around the cylinder surface (water properties at standard conditions). The validation study presented selected the lowest- and highest-Reynolds numbers configurations at the normalized gap of $G/D = 0.25$ and attempts to mimic, as nearly possible, the intended elevated fire-engulfed fuselage in the crosswind use case provided in Sec. IV. In this comprehensive section, we first present the complicated physics associated with the elevated turbulent flow past an elevated cylinder, overview the mesh and numerical approach, and proceed to overview the validation study. We note that the full set of QoIs for all LES-based models can be found in Appendix A and that the following section provides germane findings relative to the pool fire path forward, i.e., C_D and C_p.

A. Physics discussion

While our interest in elevated cylinders in crosswind are motivated by airplane accident scenarios, the underlying isothermal data set from which we draw our credibility statements for the WLMES approach are driven by the offshore pipeline use case [29]. In this often times deep-sea application, understanding detailed drag behavior as a function of pipe diameter and constructed elevation, i.e., the gap distance between the lower cylindrical surface and ocean floor, are of interest—especially as it pertains to storm surges and the required level of structural enforcement. In the classic flow past a submerged cylinder, boundary layer separation at the lower and upper surface supports small-scale vortical structures that can pair, thus forming a van Kármán vortex street that is characterized by an oscillating vortex wake (cf. visualization of this structure by Ref. [47]).

The elevated cylinder is similar to the classic cylinder in crossflow ($G/D \gg 1$), whose physics description and validation simulations can be found in, for example, Refs. [48,49]. For instance, both configurations note a "drag crisis," or the sudden drop in drag coefficient (generally from approximately 1.2 to 0.3) as a function of Reynolds number. Furthermore, the flow regimes are delineated by five classifications (subcritical, critical, supercritical, upper transition, and trans-critical regimes) where laminar to turbulent transition can be strongly affected by incoming turbulence intensity [41], while experimental facility factors such as the blockage ratio can be extremely important to QoIs

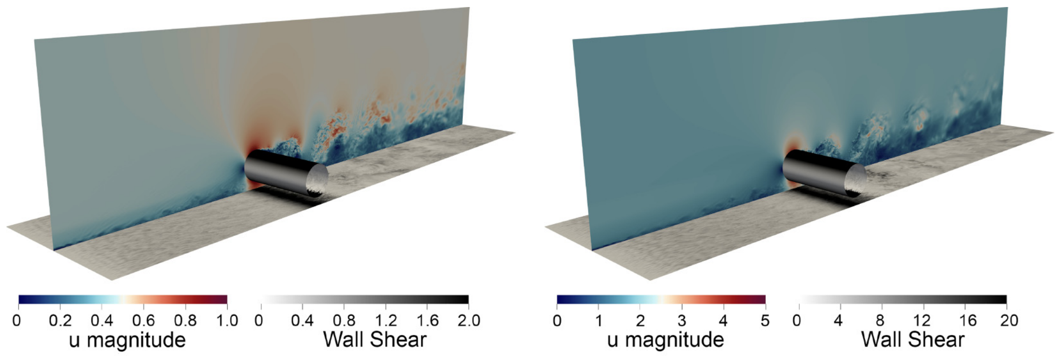

(a) (b)

FIG. 3. Velocity magnitude (vertical plane) and wall shear stress (cylinder and ground surface) shadings for the subcritical (a) and supercritical (b) configurations. The model suite depicted activated the dynamic k_{sgs} with exchange-based velocity sampling.

such as pressure distribution and Strouhal number [50]. However, marked differences are found as well—most notably the asymmetric time-mean pressure coefficient within both the subcritical and supercritical drag regime [29], upper and lower cylinder boundary layer velocity profiles (the later of which is complicated by the proximate ground plane turbulent boundary layer)—in addition to the suppression of vortex shedding at $G/D \leqslant 0.3$ in the subcritical regime [51]. For our fire use case, we will focus on the subcritical and supercritical drag regime as this complements frequency explored accident scenarios and wind speed maps [52].

In Fig. 3, a representative vertical plane and ground/cylinder surfaces with shadings of velocity magnitude and wall shear stress for the low- and high-Re_D configurations are presented. In this figure, the complex upper and lower shear layers, whose effect on the fire structure are further explored in Sec. IV, are noted as are the existence of a coherent vortex street for both regimes. The subcritical regime is characterized by a laminar boundary layer, separation, and a fully turbulent wake, while the supercritical regime is marked by a laminar-to-turbulent boundary layer transition followed by separation and, again a fully turbulent wake. Due to the proximity of the lower wall and associated growing turbulent boundary layer, a strong region of flow acceleration is found that substantially increases local shear stress directly below the cylinder.

For a representative volume-rendered visualization for the Q criterion [53], which is mathematically defined as the second invariant of the velocity gradient characteristic equation, for each flow configuration, see Fig. 4. Again, large-scale coherent vortical structures are seen in the wake of the elevated cylinder. Also seen in this set of images are the turbulent boundary layer development and the existence of hairpin vortices at the lower wall surface. We note due to the lack of laminar-to-turbulent transition model, the inability of our WMLES approach to capture proper boundary layer transition phenomena that may be able to be improved by incorporation of more sophisticated transition models [54].

B. Mesh, boundary conditions, and numerical parameters

A coarse mesh was constructed in two dimensions where the 0.196 m diameter cylinder (D) was positioned at a gap-to-diameter G/D ratio of 0.25. The upstream boundary was $7D$ from the cylinder axis and the outflow boundary was $13D$ downstream, providing a domain length of 3.92 m. The domain height was specified as 1.0 m. The near-wall mesh topology consisted of linear quadrilateral elements followed by a conformal transition to linear triangular elements. For mesh constraints, a cylinder edge sizing of 0.001 m was specified. The coarsest element size in the domain was set to 0.02 m. Inflation layers (i.e., boundary layer mesh elements) were specified on the ground and

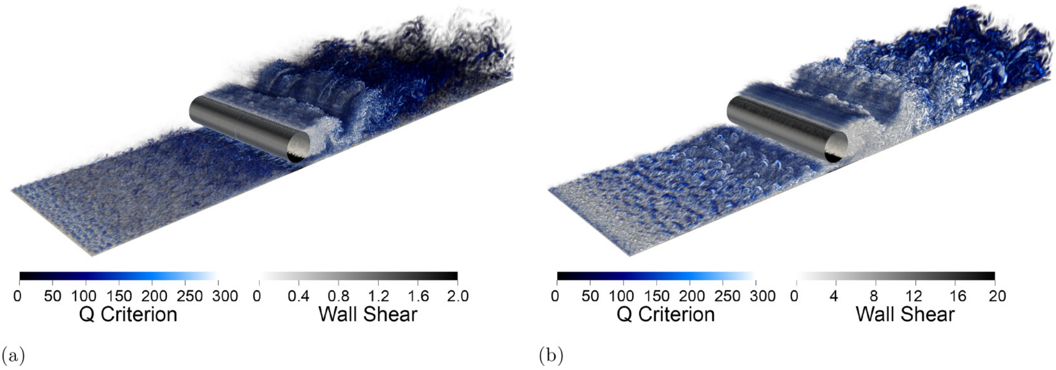

FIG. 4. Volume rendering of the positively clipped Q criterion for the subcritical (a) and supercritical (b) configurations. The model suite depicted activated the dynamic k_{sgs} with exchange-based velocity sampling. In this figure, as with all Q criterion images in this paper, we have positively clipped the field to showcase vortical structures.

cylinder surfaces. The first layer height on the cylinder was set to 0.0005 m, and the boundary layer had 40 elements with a growth rate 1.03. The ground boundary layer also had a first layer height of 0.0005 m with 16 elements and a growth rate of 1.04. Last, a sphere of influence mesh control was centered on the cylinder with a radius 0.588 m and element size 0.005 m.

The two-dimensional domain and mesh, before extrusion and mesh refinement, are shown in Fig. 5. This mesh exhibits increased resolution in and around the cylinder region and was extruded in the spanwise direction (mesh spacing 0.005 m) five cylinder diameters to yield a three-dimensional conformal hybrid hexahedron/wedge mesh. We note that our spanwise distance represents a much larger extrusion distance than previous high-fidelity studies [49] where $\pi D/2$ was used, however, preliminary coarse-mesh sensitivity studies showcased that this spanwise distance safety removed the effects of spanwise dimension. The baseline mesh was uniformly refined twice with smoothing of the curved cylinder at each refinement step. The series of mesh refinements (R) yielded an element count of roughly 9, 73, and 580 million elements for the R0, R1, and R2 meshes, respectively.

The boundary conditions used in this study included a front inflow vertical plane (steady inlet velocity profiles provided by Yang *et al.* [29] to yield a Re_D of 1.1×10^5 and 4.3×10^5 set of flow configurations), a far-field back vertical open plane where a constant static pressure was specified, a top symmetry boundary where the normal stress is applied, spanwise periodicity, and a bottom wall and cylinder no-slip algebraic equilibrium wall model as described in Sec. II. Low-dissipation Galerkin-based advection operators for momentum transport were activated, along with a second-order, three-state fully implicit time integrator (unity Courant time stepping was used for each simulation configuration). For more low-Mach discretization details, see Ref. [39]. To learn more of the generalized unstructured approach along with the suitability of the CVFEM discretization methodology that is deployed in this study for both elevated cylinder use cases, see Ref. [38].

Three-dimensional scoping simulations for the low- and high-Re_D configurations probed streamwise velocity at the lower cylindrical shear layer (a point shifted $(\Delta x, \Delta y) = (D/2, -D/2)$ from the center of the cylinder) and remarkably captured a similar Strouhal number of approximately 0.27 for both cases (0.68 and 2.61 Hz for the 0.5 and 1.87 m/s crosswind configurations, respectively). This shedding frequency was used to determine a reasonable time period to collect statistics for the production simulations. Specifically, for the R0 and R1 results, post-startup, roughly 30 shedding events were used for statistical convergence, while for the R2 mesh simulations, approximately 15 shedding events were sufficient to showcase convergence in our mean QoIs. The complete model suite variation includes the static and dynamic coefficient Smagorinsky and k_{sgs} models with both local and exchange-based velocity sampling. The exchange-based WMLES sampling used a fixed

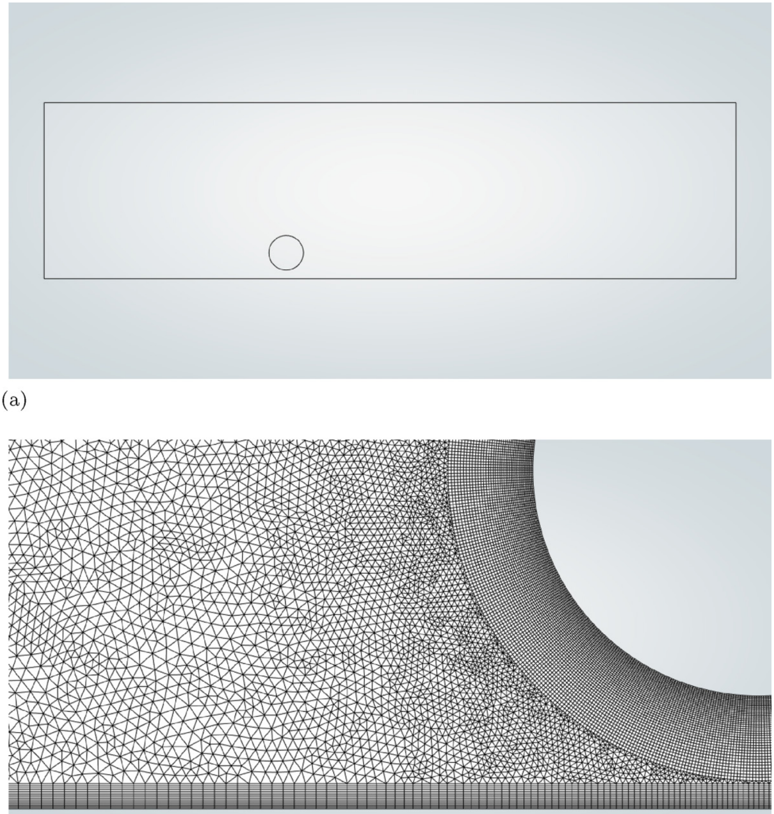

(a)

(b)

FIG. 5. Isothermal case two-dimensional (a) geometric domain and (b) the near-wall, computational mesh.

distance of 0.003 m and 0.002 m for the subcritical and supercritical configurations, respectively. Mixing local and exchange-based velocity sampling, e.g., using an exchange-based approach for the bottom wall, while using local velocity sampling for the cylinder wall, while supported in the code base, was not investigated.

In this study, a consistent set of sparse linear solver settings were used. Specifically, a generalized residual method (GMRES) was activated for all transport equations that was preconditioned by a symmetric Gauss–Seidel smoother. An aggregation-based algebraic multigrid preconditioner was activated for the continuity equation. Each of these solver strategies is supported through the Tpetra-based Trilinos open-source solver package [55]. Simulations were run on the Sandia National Laboratories Amber Institutional Cluster (2.0 GHz Intel Zeon Platinum processors; nodes with dual sockets, 52 cores each (112 cores/node); Cornelis Omni-Path interconnect). Upper computation node usage for the most refined R2 mesh was 64 (7,168 MPI ranks), that resulted in roughly eight restarts (each restart consumed 48 hours of wall time). As such, the R2 simulation over all model form variations represented a somewhat intense computationally effort.

C. Isothermal cylinder QoIs

Transient subcritical integrated drag coefficients are presented in Fig. 6 (Smagorinsky model activated), while in Fig. 7 the k_{sgs} model is depicted. Both figures include the static and dynamic coefficient procedure with local- and exchange-based velocity sampling for the subcritical configuration. Increased predictivity and excellent mesh convergence using the dynamic coefficient

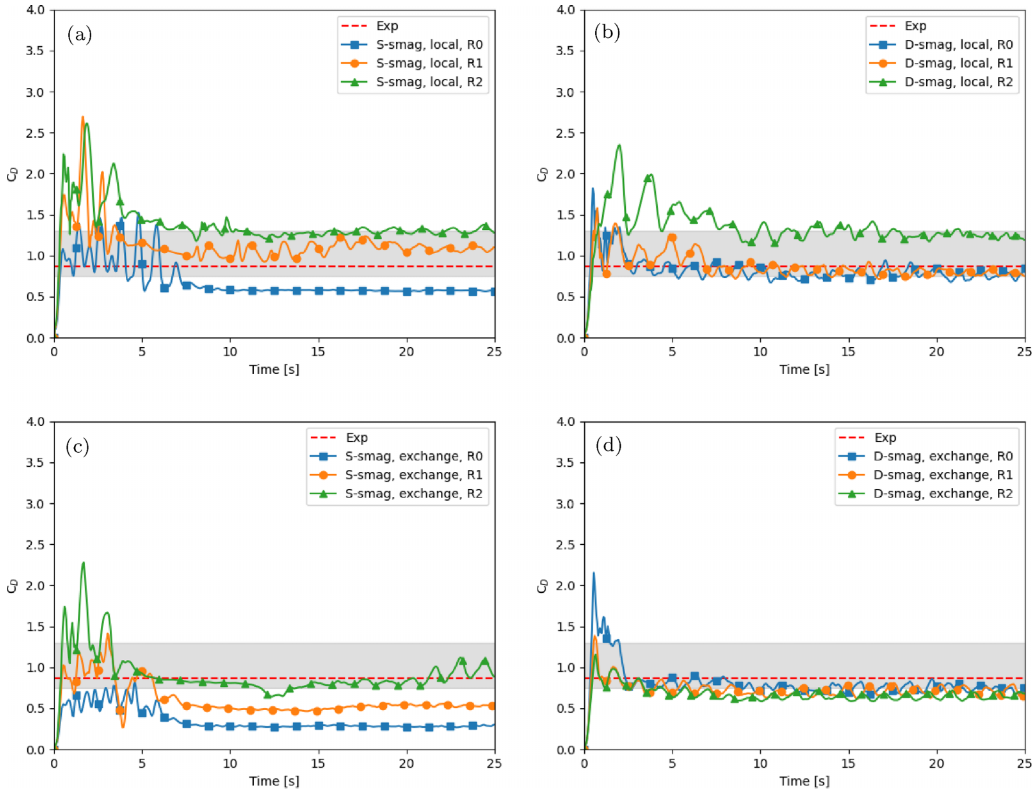

FIG. 6. Subcritical C_D as a function of time for both the static and dynamic Smagorinsky model suite (a) and (b) using local velocity WMLES sampling as compared to the static and dynamic Smagorinsky model (c) and (d) using exchange-based velocity sampling. In this panel set, as with others in this section, the R0, R1 and R2 mesh refinements are shown; S- and D- represent the static and dynamic model suite. The dotted line and shaded region represent the mean and high/low experimental values from Ref. [29].

approach are observed for both models when the exchange-based strategy is employed due to synergistic deactivation of the turbulence model in laminar regions along with the more accurate velocity sampling that forms the input to the wall model. In fact, the dynamic coefficient approach is not sufficient to showcase QoI mesh convergence. However, the dynamic procedure for both models has a greater effect on mesh convergence than does activation of the exchange-based sampling. Further exploration of the dynamic coefficient approach for the k_{sgs} concluded that the dynamic procedure for the turbulent viscosity coefficient was most important, while the dynamic approach for the dissipation closure [30] was secondary and was not a significant source of increased model predictivity.

For the supercritical configuration, transient subcritical integrated drag coefficients are presented in Fig. 8—now, only for the Smagorinsky model. Findings clearly indicate that the combination of the dynamic model along with the “fixed-in-space while refined” exchange-based velocity sampling WMLES methodology is required for both good prediction of C_D and mesh convergence. This consistent finding between the subcritical and supercritical flow regime drove a down selection for the supercritical case test suite (see Fig. 9), where the static coefficient k_{sgs} model and local velocity sampling was omitted due to overall R2 simulation expense. Good predictivity and mesh convergence are established using the dynamic k_{sgs} model along with fixed exchange-based velocity sampling. As can be seen, both models are equally performant, and (most critically) accurately captured the drag crisis while showcasing excellent mesh convergence.

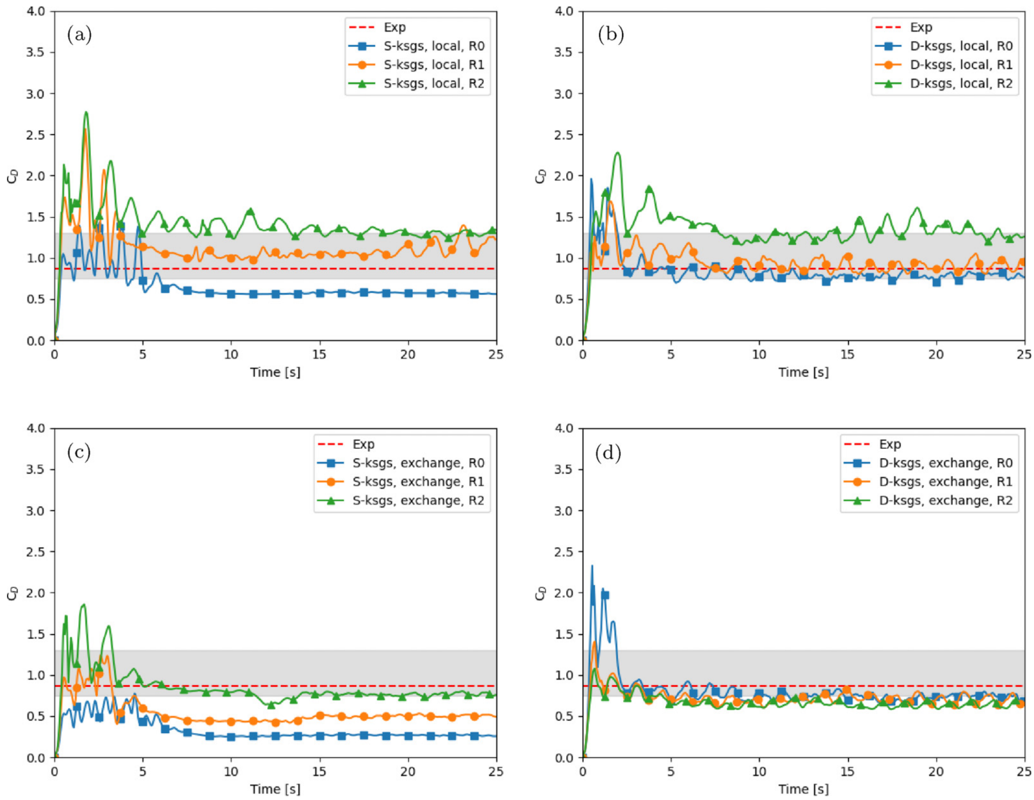

FIG. 7. Subcritical C_D as a function of time for both the static and dynamic k_{sgs} model suite (a) and (b) using local velocity WMLES sampling as compared to the static and dynamic k_{sgs} model (c) and (d) using exchange-based velocity sampling.

For QoIs at the surface of the cylinder, which first comprise of time-mean subcritical pressure coefficients as a function of angle and mesh resolution, see Fig. 10. Here, we showcase the usage of the exchange-based model where the static and dynamic model is varied for both the Smagorinsky and k_{sgs} model suite. For the exchange-based supercritical pressure coefficient plots (static and dynamic Smagorinsky model, along with dynamic k_{sgs}), see Fig. 11 (complete C_p plots can be found in Appendix A). In these figures, positive angles follow a clockwise direction; reference pressures used in C_p calculations, as reported in Ref. [29], are at the $\theta = 0^\circ$ station. Results showcase good mesh convergence and decent prediction of the boundary layer separation location when using either dynamic model suite with exchange-based velocity sampling. Reasonable C_p comparisons are presented with reduced predicted values near the 90° and 270° stations likely due to reduced wall resolution and, certainly, model-form error. We again note excellent mesh convergence when using the dynamic model and exchange-based velocity sampling.

Finally, we showcase the time-mean, untransformed law-of-the-wall, wall-normal dimensionless quantity, y^+ for the subcritical and supercritical drag regime—showcasing the exchange-based velocity sampling that is held constant as the mesh is refined (Smagorinsky and k_{sgs}) in Fig. 12.

IV. FIRE-ENGULFED OBJECT SUBJECTED TO CROSSWIND

In the experimental study of Ref. [3] (experiments #6 and #7), a capped culvert (diameter approximately 4 m; outer steel and inner insulation thickness of 1 mm and 4 cm, respectively) was elevated 0.6 m from an $\mathcal{O}(10)$ m-diameter pool fire consisting of JP-8. The backside of this culvert,

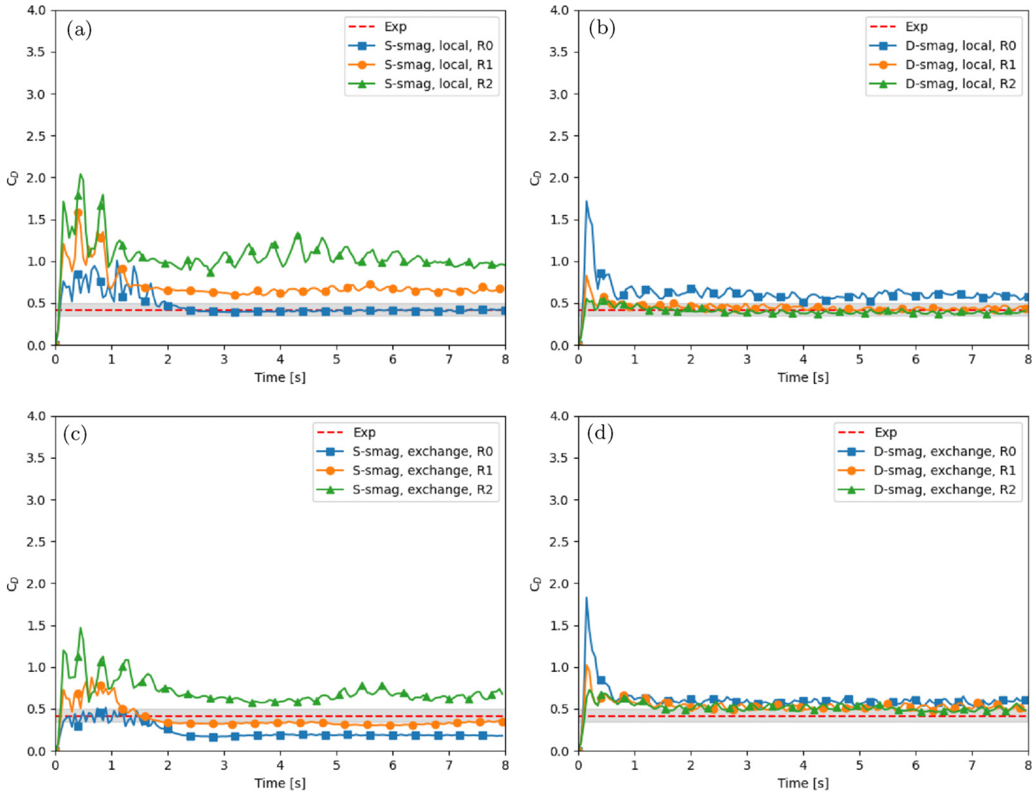

FIG. 8. Supercritical C_D as a function of time for both the static and dynamic Smagorinsky model suite (a) and (b) using local velocity WMLES sampling as compared to the static and dynamic Smagorinsky model (c) and (d) using exchange-based velocity sampling.

whose diameter was meant to replicate an airplane, i.e., a "mock fuselage," was placed tangential to the leeward edge of the pool and subjected to an outdoor environment that corresponded to a low- and a high-crosswind configuration (experiment #7: 2.0 m/s, and experiment #6: 9.5 m/s,

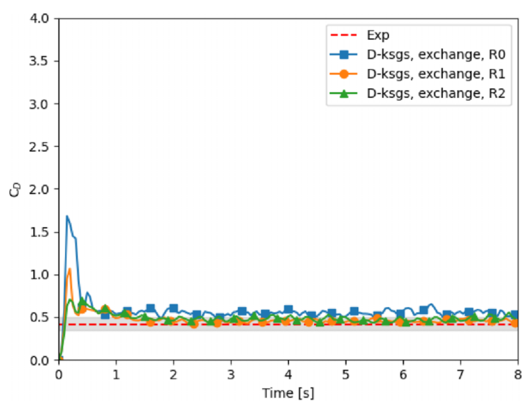

FIG. 9. Supercritical C_D as a function of time for the dynamic k_{sgs} model using exchange-based velocity sampling.

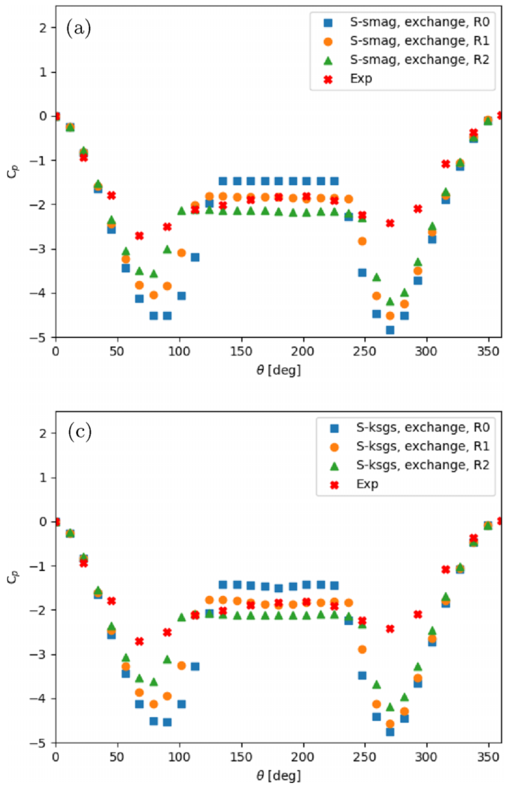

FIG. 10. C_p for the subcritical regime as a function of angle, including both the static and dynamic Smagorinsky model suite (a) and (b) as compared to the static and dynamic k_{sgs} model (c) and (d), shown with experimental results from Ref. [29]. All simulation results showcase the exchange-based velocity sampling.

respectively). Flame shapes (through black and white temperature shadings) were provided via a lattice of thermocouples, in addition to peak incoming radiative flux, or irradiation. For the 2.0 m/s configuration, the experiment found that the flame was firmly attached at the windward cylinder location, whereas for the high-wind crossflow configuration, the flame migrated to below the cylinder and was fully attached at the leeward cylindrical surface. Moreover, peak instantaneous irradiation measurements were roughly 200 and 220–320 $\mathrm{kW/m^2}$ for the low- and high-crosswind configurations, respectively. An interesting aspect associated with this study as compared to the isothermal study is rampant flame intermittency that occurs over the engulfed cylindrical object. Whereas in the isothermal case where a fixed set of properties are appropriate, in this application—depending on the state of fuel reaction and proximity to the object—the identified Reynolds number can vastly fluctuate. Moreover, in outer regions of the cylinder, the Reynolds number can exceed the supercritical regime and, for the high-crosswind configuration approach the transcritical regime. However, for flame attached regions of the object, the previously validated isothermal Reynolds number ranges are complementary.

In this comprehensive section, we follow the same approach captured in Sec. III where, first, a physics description of the fire-engulfed object in crosswind is presented. Next, meshing and numerical parameter details are presented, followed by a set of QoI results that include flame dynamics, time-mean flame shape as a function of crosswind, and global heat flux comparisons between experiment and simulation. Due to the size and complexity of the fire environment, detailed temperature and velocity profiles are not available. Moreover, due to the changing direction and intensity of the outside wind profile, predicted values of radiative and convective heat fluxes include

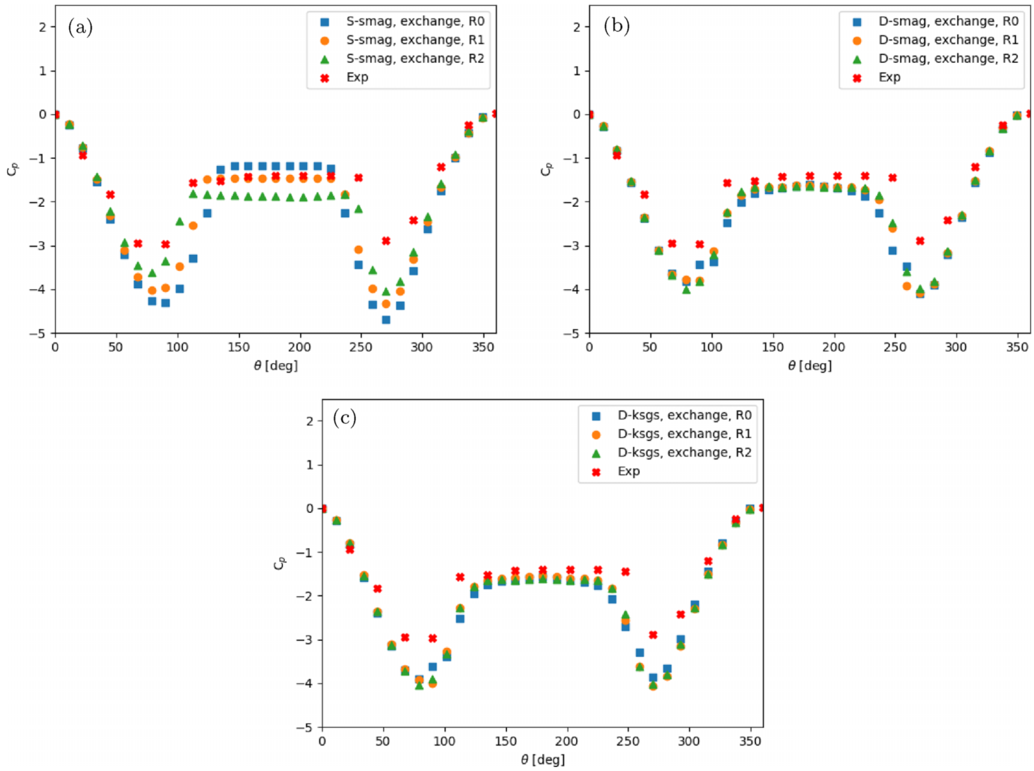

FIG. 11. C_p for the supercritical regime as a function of angle, including both the static and dynamic Smagorinsky model suite (a) and (b) as compared to the dynamic k_{sgs} model (c). All simulation results showcase the exchange-based velocity sampling.

possible errors that arise from choosing a constant inflow direction as opposed to resolving the spatiotemporal physical inlet profile captured in Ref. [56] that varied over 800 s.

A. Physics discussion

Figure 13 provides an instantaneous mixture fraction (i.e., fuel), shading associated with a vertical pool-centerline cut-plane in the low- and high-crosswind configurations. The figure captures the expected upper and lower shear layers that are responsible for enhanced mixing of the fuel and air within the turbulent wake of the cylinder. Owing to the low inlet pool velocity, genesis of the induced vertical velocity is from combustion-driven buoyant acceleration. Also present is evidence of baroclinic torque generated vortical structures that can be seen just above the pool surface. When the velocity induction is sufficiently high relative to the incoming momentum field, fuel breaches the upper cylindrical surface, whereas for high incoming momentum, as is present for the 9.5 m/s configuration, the fuel is pushed largely toward the lower cylindrical surface. The intermittent generation of pool fire fingerlike structures along with large-scale puffing events, which will be further showcased in Sec. IV C, support fuel in the high-crosswind configuration to breach the upper cylinder shear mixing layer, thus resulting in flames briefly enveloping the upper cylindrical surface. As investigated in Ref. [9], the role of an incoming turbulent boundary layer on flame dynamics was evaluated. Results showcased that the pool fire substantially alters the burst-sweep cycle and, in fact, the pool is responsible for a substantial amount of turbulence production. As such, the role of bypass transition, i.e., the circumvention of the standard laminar-to-turbulent boundary

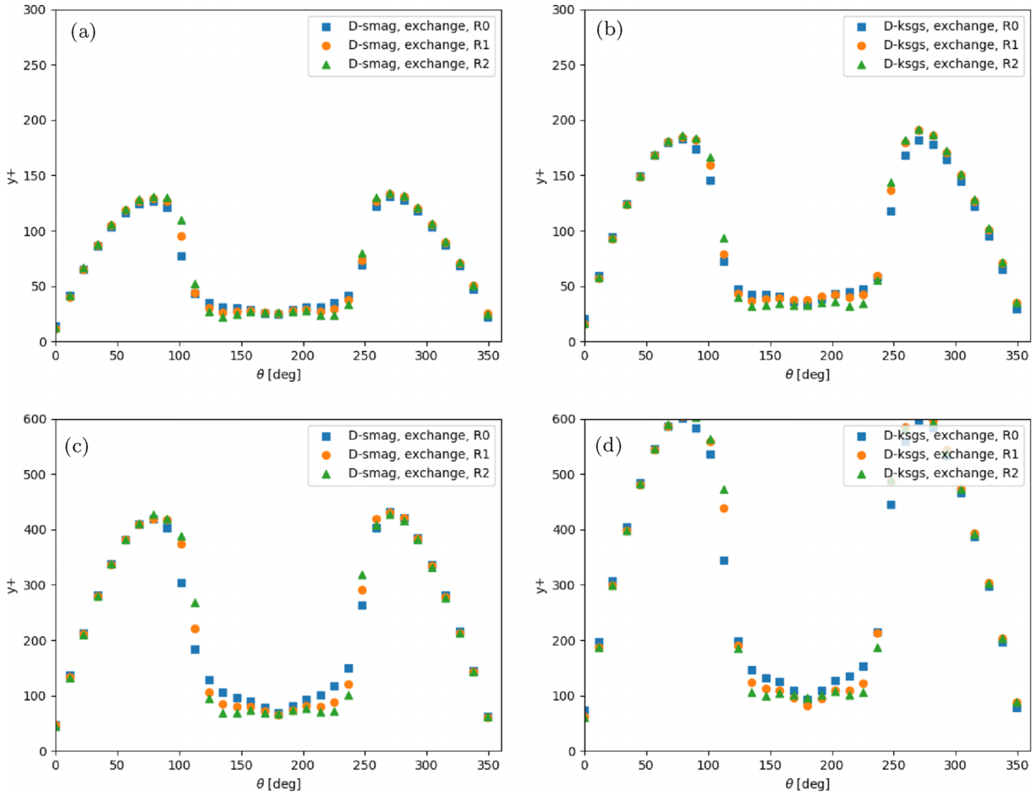

FIG. 12. Dynamic Smagorinsky and dynamic k_{sgs} model suite y^+ as a function of angle for the subcritical (a) and (b) and supercritcial (c) and (d) regime.

layer transition on the cylinder surface, is expected to be an easing effect associated with this validation study.

In Fig. 13, for both the low- and high-crosswind configurations, windward generation of shear layer vortical structures (via a baroclinic torque mechanism) interact with upper- and lower-cylinder shear layer structures (in the presence of boundary layer separation) to drive improved mixing and, thus, combustion efficiency. In Ref. [3], the increased fuel/air mixing was sited as the motivation for increasing surface mean incoming radiative heat flux as crosswind escalates, along with migration

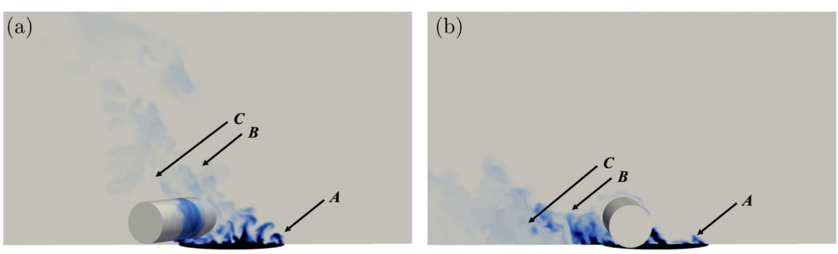

FIG. 13. Vertical plane depicting mixture fraction shadings for the low- (a) and high-wind (b) configurations. The figure also includes the mock fuselage and pool surface, for which instantaneous mixture fraction shadings are also provided. Small-scale plume structure, along with the upper- and lower-shear layers identification are labeled as (A), (B), and (C), respectively.

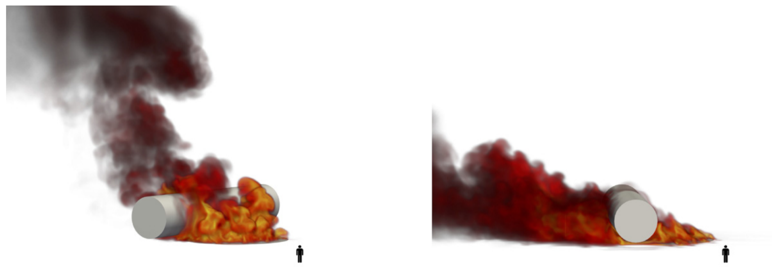

(a) (b)

FIG. 14. Volume-rendered temperature field for the low- (a) and high-wind (b) configurations. The figure also includes a constant shaded mock fuselage and pool surface. A representative human depiction is provided for size perspective.

of the attached flame from the windward to leeward surface of the cylinder. A representative volume-rendered instantaneous temperature field at the mixture fraction instantaneous state shown in Fig. 13 is presented in Fig. 14, highlighting the discussion above, where intermittent penetration of fuel above the cylinder (for the high-crosswind configuration) is captured. For the low-crosswind configuration shown in Fig. 14, the flame is seemingly enveloping the entire central core of the mock fuselage. This finding will be further explored in Sec. IV C where the transient flame structure for both configurations is explored.

A notable complexity associated with the low-crosswind configuration is the presence of substantial yaw. As will be highlighted in the fire meshing section, see Sec. IV B, the 2.0 m/s crosswind experiment was conducted using a mean crosswind velocity impingement of -36° yaw. As described in Matsumoto *et al.* [57], the presence of yaw in a cylinder-in-crosswind configuration results in an enhanced Kármán vortex structures occurring at the upper, or windward cylinder location. Moreover, axial vortex structures are formed and move along the yawed object with highly disparate velocity fluctuations [58]. Wind tunnel experiments, which were conducted by Cheng *et al.* [59], also measured excitation of shedding frequencies due to yaw in the supercritical drag regime. While this complex vortical field was not addressed in the experiments of Ref. [3], this break in symmetry of the flow past the elevated fuselage is expected to have a substantial affect on centerline QoIs such as flame shape and incident radiative heat flux. We note that while this flow phenomena has been linked to increased vibration for yawed cables exposed to crosswind, the vibrational spectrum of the disparate shedding structures over our mock fuselage is not of direct interest to the study. Nevertheless, the flow physics of a yawed elevated cylinder in crosswind subjected to fire represents a critical credibility gap to close given the ubiquity of wind direction relative to damaged stationary transportation vehicles.

B. Mesh, boundary conditions, and numerical parameters

As described in the introductory statement of this section, due to varying experimental wind conditions relative to a fixed-in-place capped mock fuselage, the production meshes used a -36° and 2° yaw for the low- and high-wind configurations, respectively. Mean inflow conditions were chosen due to the unaffordable computational time that would have been required to model the 800 s experimental inflow wind data. The three dimensional hybrid, conformal topology meshes exercised in this study consisted of linear Wedge6 and Tet4 elements. Solid modeling and meshing were performed in ANSYS Workbench. An overhead view of the computational domain can be seen in Fig. 15. In the small pool experimental set, the pool diameter, D_p, is 9.45 m. The mock fuselage outer diameter was 3.66 m, and the length, L_f, was 18.29 m. The fuselage axis was 2.43 m above the ground leaving a gap of 0.60 m. The back edge of the ribbed culvert was aligned with the edge of the pool as shown in Fig. 15 and clearly highlights the two different

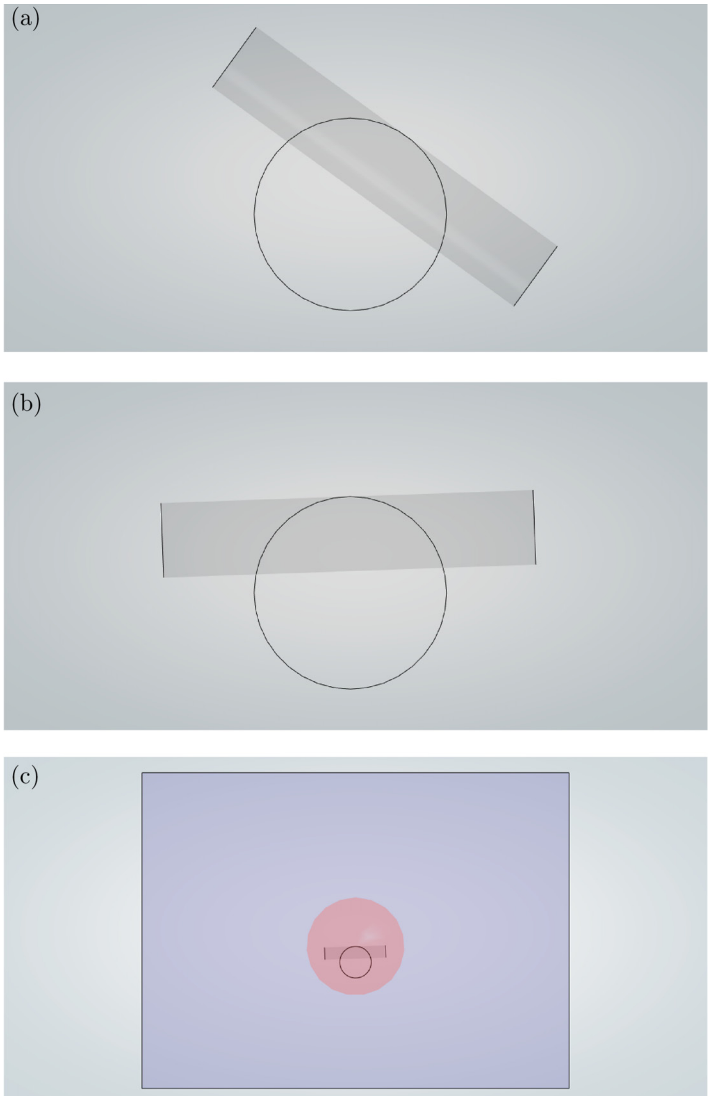

FIG. 15. Overhead views of the computational domain for the low- (a) and high-wind (b) configurations, including outlines of the cylinder and pool. In panel (c), the sphere of influence used for local mesh refinement is depicted by a shaded region in proximity to the pool and cylinder (shown for the high-wind configuration).

yaw angles. The computational domain had a width equal to $7L_f$, a depth of $10D_p$, and a height of $4D_p$. The center of the pool was $4D_p$ from the inflow boundary and $6D_p$ from the outflow boundary.

Meshing was performed with a minimal number of specified size constraints. For the coarsest mesh, R0, the maximum characteristic domain body sizing was set to 2.0 m. This parameter effectively determines the far-field mesh resolution. An additional sphere of influence body size constraint was added to increase mesh resolution around the mock fuselage and pool. The sphere of influence was centered at the back edge of the pool, had a radius of 15.0 m, and a size constraint of 0.4 m. This procedure ensured more refined elements in the wake of the mock fuselage. An overhead view of the sphere of influence is also shown, in red, in Fig. 15(c). Inflation layers (i.e., boundary layer mesh elements) were added near the ground and culvert surfaces. In the coarsest mesh, R0, two layers were prescribed with a growth rate of 1.2 and a maximum thickness of 0.4 m. The maximum boundary layer thickness was assigned so the ground and cylinder inflation layers would not overlap, and also provide sufficient space for a layer of tetrahedral elements between the two wedge-based boundary layer extrusions. Such an approach highlights the flexibility associated with a generalized unstructured approach, while noting that a hexadral-based mesh with transition elements (pyramids) to a block of tetrahedra was also possible, yet proved more expensive to construct by way of person-hours.

For the first mesh refinement, R1, domain body sizing was set to 1.0 m. The size and location of the sphere of influence was the same but the mesh sizing near the fuselage and pool was 0.2 m. The maximum thicknesses of the boundary layers on the ground and cylinder surfaces, and the growth rate was the same, but the number of layers was doubled to 4. For the second mesh refinement, R2, the domain body sizing and sphere of influence body sizing were reduced again by a factor of 2 to 0.5 m and 0.1 m, respectively. The maximum thicknesses of the boundary layers on the ground and cylinder surfaces, and the growth rate were the same, but the number of layers was doubled again to 8. Images of all three mesh resolutions are shown in Fig. 16. Mesh refinements were performed in the meshing tool itself, unlike the previous isothermal cylinder section that carried out uniform refinement with geometry smoothing. The approach exercised in the fire simulation captures curvature naturally within each successive refinement, while exact uniform refinement patterns are not guaranteed, e.g., a Wedge6 element type need not be uniformly refined to eight new elements. Therefore, total mesh counts of approximately 2, 13, and 102 million elements for the R0, R1, and R2 refinement levels, respectively, were generated.

Using the lessons-learned from the isothermal elevated study, the dynamic coefficient k_{sgs} model is activated in concert with the exchange-based equilibrium wall model as described in Sec. II. This baseline model algebraically closes the scalar variance, $\widetilde{Z''^2}$, which is computed from resolved mixture fraction gradients, $\widetilde{Z''^2} = C_V \Delta^2 \frac{\partial \tilde{Z}}{\partial x_i} \frac{\partial \tilde{Z}}{\partial x_i}$, where C_V is statically set as 0.5 [30]. Code stability issues prevented the dynamic coefficient approach to be applied for C_V when using the algebraic formulation. Ongoing physics-based model form fire validation studies are evaluating a transport-based equation for scalar variance as demonstrated in Ref. [60] where increased stability is noted with using a dynamic procedure. However, we view this path germane to upcoming structural uncertainties associated with the underlying physics modeling approach as first established in Ref. [7].

The boundary conditions used in this study included a front inflow vertical plane (steady inlet power-law velocity profiles provided in Ref. [3]), a far-field back vertical open plane where a constant static was specified, a top open boundary with a far-field tangential velocity and constant static pressure specification, spanwise periodicity, and an equilibrium wall function (using exchange-based velocity sampling) for the bottom wall, pool, and cylinder surface. As followed in Domino [9], a wall mass injection was applied where the temperature (488.15 K) and velocity (mass flux of $0.03\,\text{kg/s/m}^2$) is used to inject momentum and species into the domain.

Low-dissipation Galerkin-based advection operators for momentum transport, whereas a gradient reconstruction-based upwind approach for scalar transport, which activates a van Leer limiter, and a second-order, three-state fully implicit time integrator are again activated. As with the isothermal study, unity Courant time stepping was used. The second-order implicit time integrator yielded good stability in this highly nonlinear physics set. For PMR, 128 ordinate directions were activated (T_4) and, due to the highly unstructured mesh configuration consisting of tetrahedral- and wedge-based elements topologies, activated a CVFEM-based Streamwise Upwind Control Volume (SUCV) stabilization approach as highlighted in Ref. [7] rather than an edge-based vertex-centered SUCV stabilization (as shown in the verification section of Ref. [7], both are design-order accurate). A sooting heptane fuel was used as a JP-8 surrogate. Conjugate heat transfer coupling with the

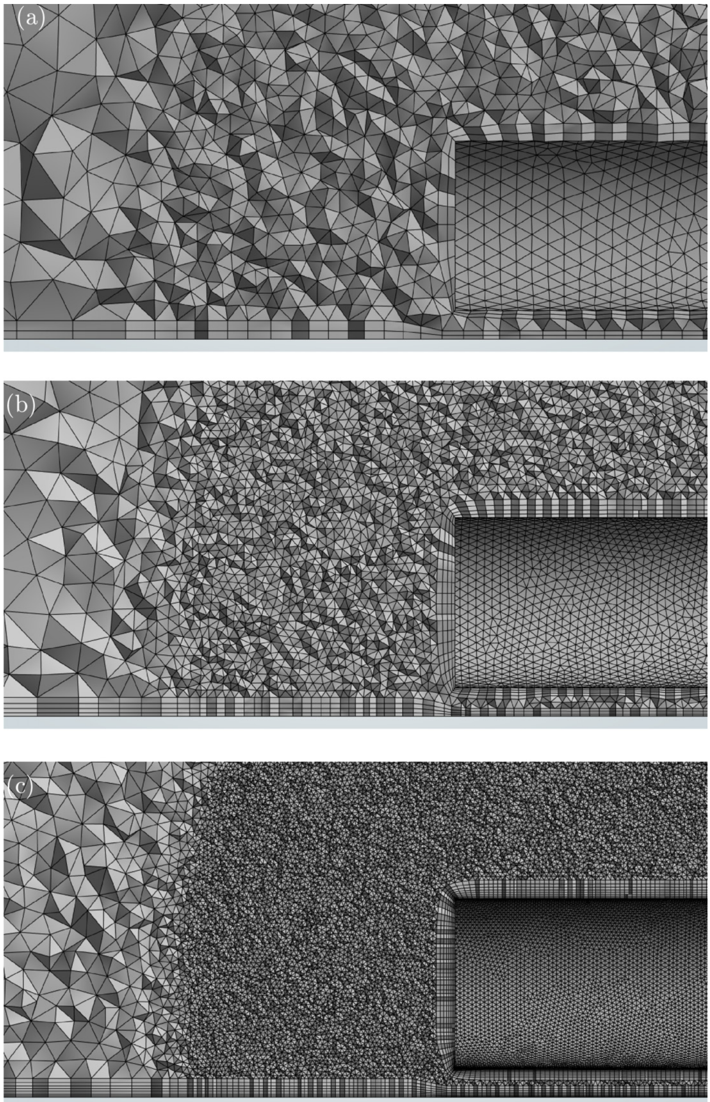

FIG. 16. Mesh views at spatial resolutions of (a) R0, (b) R1, and (c) R2.

culvert included an outer quadrilateral shell element followed by a hexahedron insulation block that replicates the experimental setup, while noting internal structural features were neglected. Enclosure radiation was included at the interior annulus of the culvert, where Sierra/Aria computed the transient thermal response [45].

For the R0 and R1 results, 120 s of physics time was modeled, while for the R2 study, $\mathcal{O}(70)$ s were used for the low- and high-crosswind configurations. The finest mesh yielded $\mathcal{O}(35)$ puffing cycles for a representative timescale based on diameter [61] and quiescent flow. Our latest study captures far more physical simulation time that has been used in our previous high-fidelity simulation studies where $\mathcal{O}(30)$ s was targeted. The exchange-based WMLES sampling used a fixed normal distance of 0.05 m for the pool and bottom surface, while 0.01 m was used for the cylinder surface. These values were used for all mesh resolutions, yielding a maximum nontransformed Favre-averaged normal distance inner unit (y^+) over the cylinder of approximately 170 and 450 for the R2 mesh (low- and high-crosswind, respectively). In each of the simulations, the maximum realized y^+ was $\mathcal{O}(500)$. The PMR mesh activated for each refinement study matched the fluids mesh and did not exploit volumetric mesh transfers between disparate mesh resolution meshes. For the thermal heat conduction region, a fixed mesh size of approximately 650 K hexahedral-based elements was used, resulting in $\mathcal{O}(200)$ k internal facets, i.e., rows in the approximately 48% dense system, with $\mathcal{O}(300)$ k internal nodes used for the internal enclosure radiation (ER) solve. Due to the large size of this system, the ER solve activated a stiff GMRES solver preconditioned by a domain decomposition incomplete lower- upper that activated a domain overlap level of two. Fluids and PMR linear solver settings were identical to those specified in the isothermal simulation study.

Simulations were again run on the Sandia National Laboratories Amber Institutional Cluster. For the most refined mesh, including the multiphysics coupling between fluids, PMR, and solid heat conduction/ER, roughly eight restarts (each restart consumed 48 h of wall time) were processed. Due to lower cluster priority, the fine mesh activated 32 nodes (3584 MPI ranks), while the R1 and R0 followed the optimal scaling node count of 16 and 2 (1729 and 224 MPI ranks, respectively).

C. Transient evolution of fire structure

As overviewed in Tieszen [62], quiescent pool fires include a range of fluid mechanics instability including Rayleigh/Taylor instabilities, i.e., bubble/spike phenomena that occur due to heavy fluid over light fluid, and can also be observed in low-Atwood number nonreacting buoyant plumes [63]. The formation of small-scale vortical structures at the outer lip of the pool contribute to overall core collapse. Baroclinic torque, which is formed by misaligned density and pressure gradients drive large scale vortical rings that contribute to repeated puffing of the pool fire, whose frequency, f, is correlated with pool diameter [61] via $f = 1.5/\sqrt{D_p}$. Vertical acceleration of the pool supports lateral entrainment and forms fingerlike structures that originate at the outer diameter of the pool (see Domino *et al.* [7] for the overview of quiescent pool fire puffing where high-fidelity LES is used to further explore fire dynamics). As highlighted in Scott and Domino [8], the addition of crosswind supports additional structures such as standing column vortices at the outer lateral edge of the pool, horseshoe vortex structures at the windward lip of the pool, and large-scale counter rotating vortex pairs—all indicative of classic jet-in-crossflow behavior [64].

To compare and contrast fire-engulfed objects subjected to crosswind with previous quiescent and nonbluff body fire environments, the transient puffing structure for the 2.0 configuration is captured in Fig. 17 (shown is volume-rendered temperature). For this 2 m/s configuration, a clear puffing transient advancement can be seen. Specifically, the sequence of images begins with a mostly attached flame over the full pool surface. At the beginning time plane Fig. 17(a), the object's central core is engulfed. This large-scale vortical feature further entrains fluid at the windward of the pool supporting a slightly lifted flame structure at the upwind pool lip. As the large-scale structure accelerates upward, fine strands of flame impinge on the windward side of the mock fuselage, while wrapping above and below the elevated culvert. Due to excessive yaw, an axial vortical flow in the downwind, angled direction of the cylinder drives an asymmetric flame attachment on the structure. In Fig. 17(k), with the large-scale vortical structure far above the pool and object, fine flame structure reattaches on the object toward the downwind direction and prepares for another puffing structure to form. Now, fire rolls over the elevated object, and is advected downstream. We note that this puffing sequence [Figs. 17(a)–17(1)] spans roughly 4 s. This sequence is roughly 2× longer than a typical quiescent pool fire of the same size and highlights the effect of the object prolonging the large-scale flaming vortical structures near the pool surface. Finally, while there are intermittent time planes where the flame is fully engulfing the windward and leeward cylinder, it mostly appears that the flame is firmly attached on the windward side. Further investigation of time-mean flame structure will be outlined in Sec. IV D.

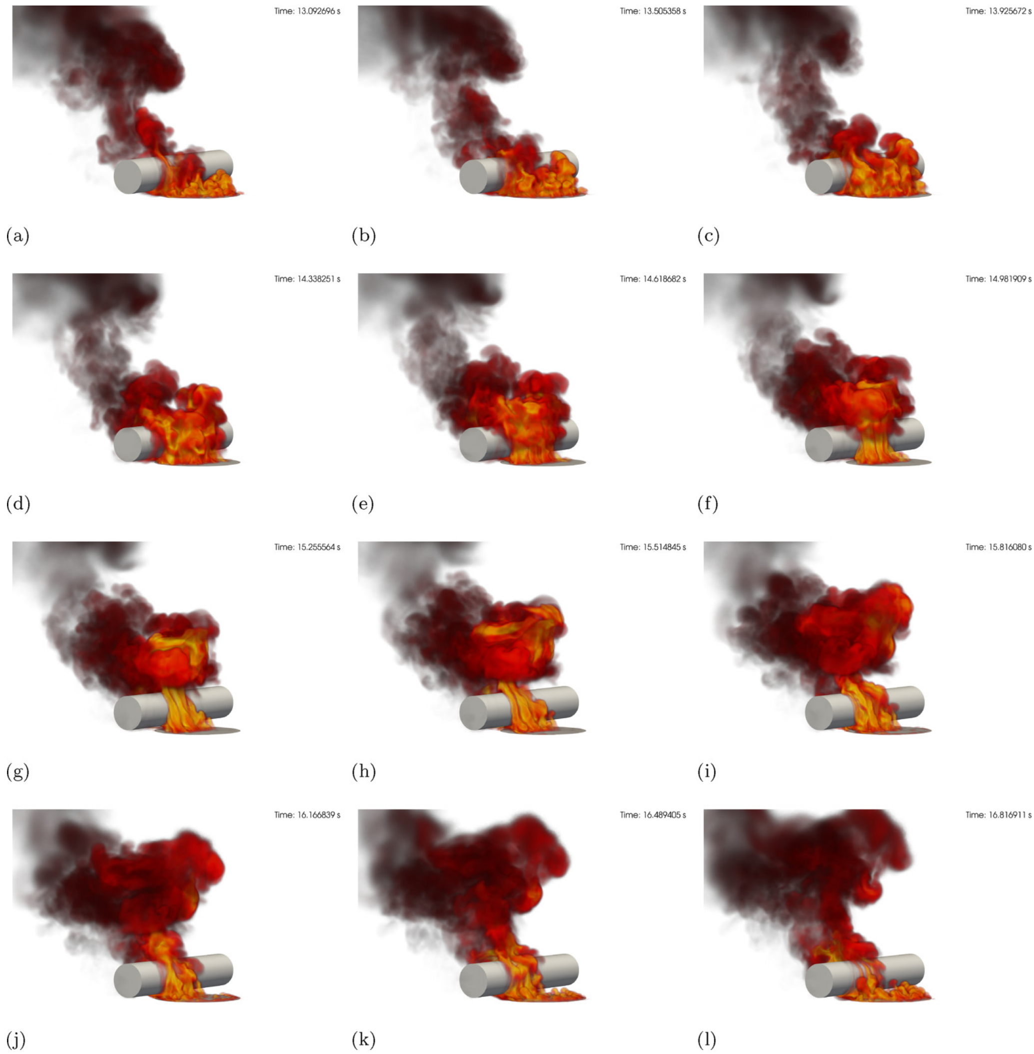

FIG. 17. Puffing cycle for the 2.0 m/s configuration.

For the high-crosswind case of 9.5 m/s transient flame structure advancement, the reader is referred to Fig 18. In this sequence of images, no apparent single, large-scale vortex ring is observed. Rather, the key flow feature of note is the formation of a small-scale fingerlike windward flame structures at the leading edge of the pool that are advected downwind. It can be seen that intermittent flame structure penetrates the upper cylinder mixing layer where fire is carried up and over the mock fuselage. These fingerlike structures continually appear at the windward pool lip, not unlike what is seen in quiescent flows, however, no coherent large-scale vortical ring is found due to the strong advection toward the leeward side of the pool. The effect of this intermittent shedding over the top of the cylinder suggests that the predominant heat flux to the object occurs under and toward the leeward side of the cylinder. Again, further investigation of time-mean flame structure will be outlined in Sec. IV D, while a volume-rendered temperature movie is provided in the Supplemental Material to this paper [65].

For novel flow features associated with fire-engulfed object physics in crosswind—now including the apparent formation of wake vortices—see Fig. 19. In this image set, the volume-rendered

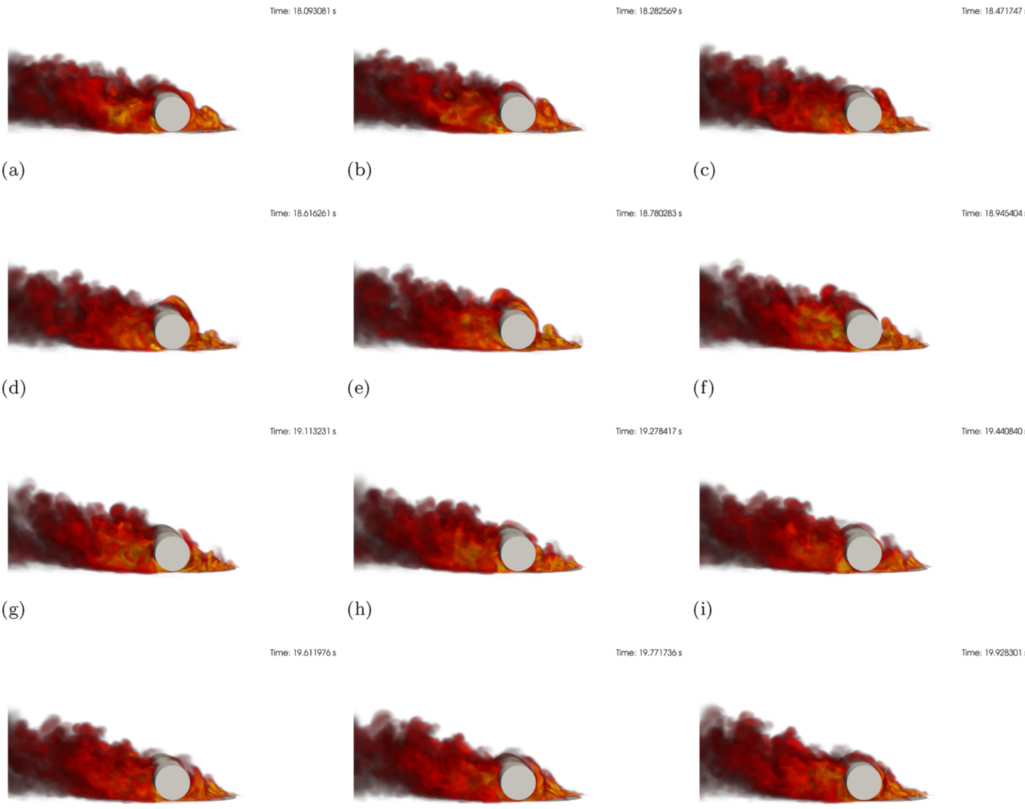

(a) (b) (c) (d) (e) (f) (g) (h) (i) (j) (k) (l)

FIG. 18. Puffing cycle for the 9.5 m/s configuration.

Q criterion images are provided for both the low- and high-crosswind configurations. For the low-crosswind configuration, several interesting flow features are noted that, to our knowledge, have not been captured in any previous fire simulation study. The presence of wake vortices in large-scale pool fire outdoor experiments were cited in Ref. [66] and can be seen in our low-wind configuration image, specifically, on the leeward side of the mock fuselage. As overviewed by Fric

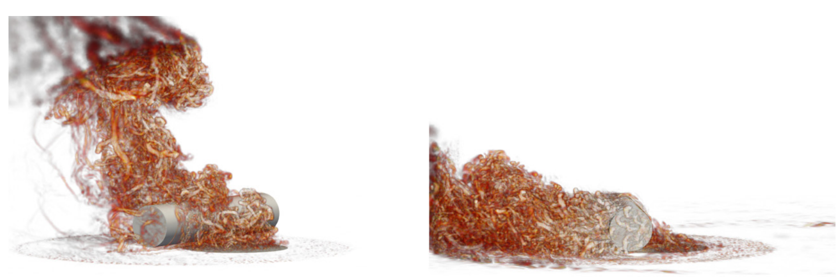

(a) (b)

FIG. 19. Volume-rendering of the positively clipped Q criterion for the low- (a) and high-wind (b) configurations. For the low-wind configuration, evidence of wake vortices are captured along with a standing column vortex (a vertical vortical structure) that meanders about the front face of the capped culvert can be seen (see supplemental Q criterion animations for more detail).

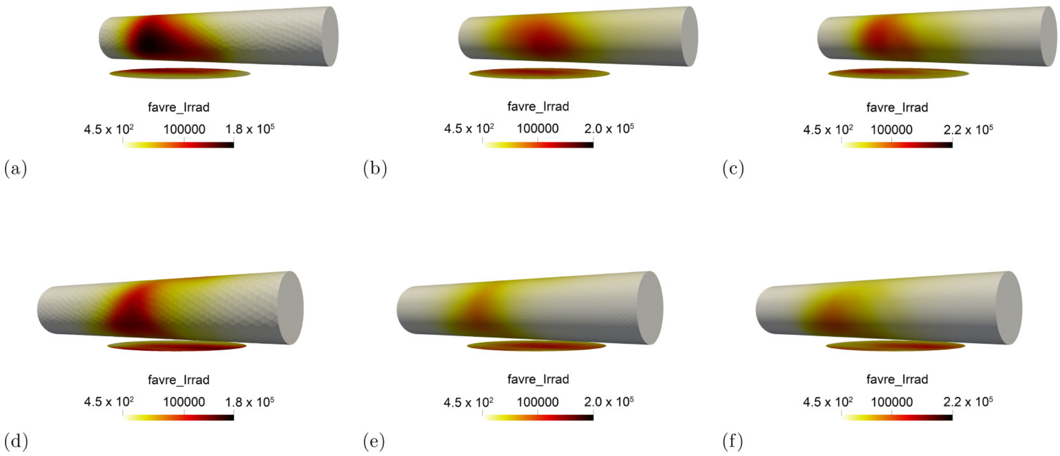

FIG. 20. Surface shadings of the incident radiative flux [windward perspective: (a), (b), (c); leeward perspective: (d), (e), (f)] for the 2 m/s crosswind configuration. The columns (a), (d), (b), (e), and (c), (f) represent R0, R1, and R2, respectively.

and Roshko [67], wake vortices are caused by interaction of the turbulent boundary layer and the wake of a jet where counter rotating vortex pairs contribute to the entrainment of vortical structures. In Tieszen *et al.* [66], these wake vortices where serendipitously visualized by the entrained dust of the China Lake desert surface, while in our visualization, the volume-rendered Q criterion seemingly captures this structure. While nonreacting jet-in-crossflow simulation images captured in Ref. [64] showcased the numerical finding (for more details, see Fig. 18(b) of Mahesh [64], where isosurfaces of Q criterion note the appearance of wake vortices), we again stress that for the large-scale fire use case, such numerical findings have not be recorded. Further investigation of the low-wind configuration showcases a standing column vortex directly to the side of the mock fuselage. This transient column vortex structure displayed a long lifetime—as can be seen in the supplemental Q criterion animation provided. For the high-crosswind configuration Q criterion image, equally rich flow features can be seen within the pool, intermittently over the top surface of the culvert, and a substantial turbulent wake region. For completeness, the effect of uniform refinement on macroscopic fire features can be found in Appendix B.

D. Fire QoI results

In this section, fire QoIs including incident radiation flux onto the mock fuselage, centerline time-mean flame contours, and quantitative comparisons with the experimental data set are provided. Time-mean incident radiative flux fuselage shadings are presented for the 2 m/s configuration in Fig. 20. In this sequence of images, the perspective for the windward view [Figs. 20(a)–20(c)] appears further away than the leeward view [Figs. 20(d)–20(f)] due to the longer entrance region to the pool, and the desire for the pool surface to be the same visual size. The shadings of the temporally averaged incident radiative flux again highlight the effect of yaw in that the flame shape is skewed to the downwind side of the culvert. Peak mean incident radiative flux appears on the windward side of the object and is $\mathcal{O}(220)\,\mathrm{kW/m^2}$. As the mesh is refined, mean radiation flux increases. However, regions of flame attachment on the cylinder appear on both the windward and leeward side of the object.

For time-mean incident radiative flux surface shadings for the 9.5 m/s configuration, see Fig. 21. In this image set, like Fig. 20, the pool surface is kept at the same visualization size, while again noting the elongated entrance region that makes the perspective of the object appear smaller from the windward view. In the high-wind configuration, the flame has clearly migrated to the

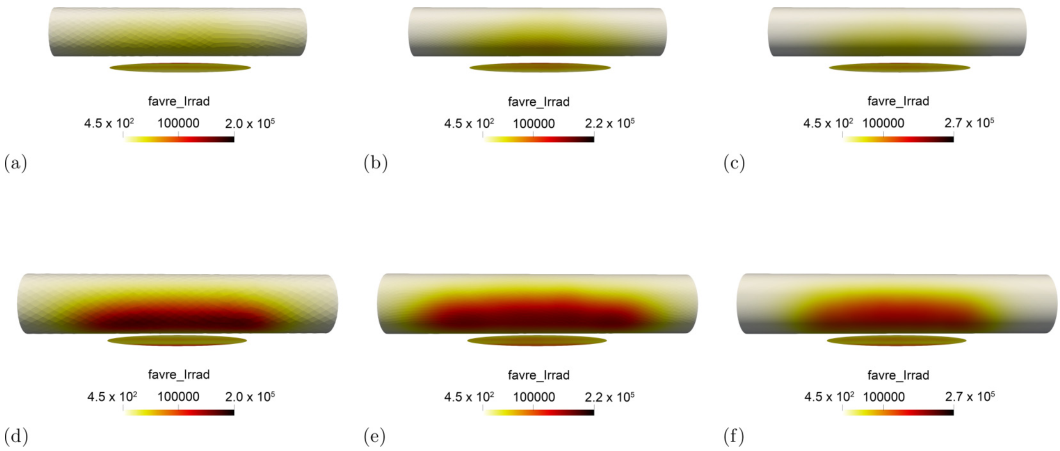

FIG. 21. Surface shadings of the incident radiative flux [windward perspective: (a), (b), (c); leeward perspective: (d), (e), (f)] view for the 9.5 m/s crosswind configuration. The columns (a), (d), (b), (e), and (c), (f) represent R0, R1, and R2, respectively.

leeward mock fuselage surface, appears mostly symmetric due to the low amount of yaw, and notes a peak value of $\mathcal{O}(270)\,\mathrm{kW/m^2}$. Again, radiative flux increases as the mesh resolution increases.

Centerline mean flame contours that showcase the migration of flame attachment from the windward to leeward location of the mock fuselage as crosswind is increased, as experimentally reported in Ref. [56], are shown in Fig 22. The Favre-averaged temperature fields also showcase a marked reduction for the low-crosswind configuration at the centerline due to the fuselage yaw. As described in the transient evolution volume renderings of temperature for the lower crosswind configuration (see Fig. 17), transient puffing events over the cylinder body intermittently engulf the fuselage while migrating toward both the windward and the left cap of the fuselage. While high temperature regions impinge and are advected over the upper side of the fuselage, they are averaged out, thus reducing the time mean gas phase temperature substantially. Our findings are consistent with conclusions provided in Ref. [56], where the tradeoff between windward buoyancy, which

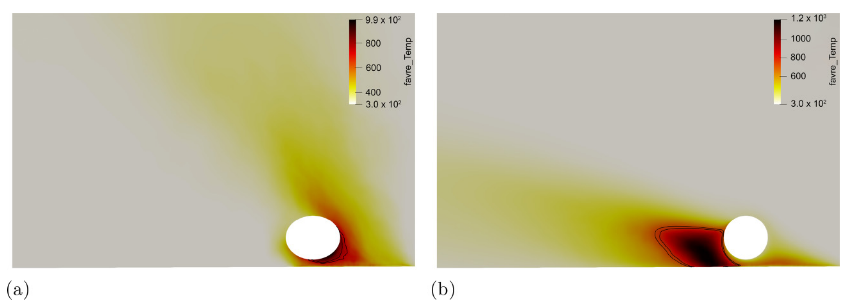

FIG. 22. Surface shadings of temperature (R2 mesh) along with flame contours for the 2.0 m/s (a) and 9.5 m/s (b) crosswind configurations at the centerline of the pool. In this image set, we follow [8,9] where the flame sheet is defined between 723.15 and 773.15 K. Strong attachment to the windward cylinder surface is observed for the low-crosswind configuration, whereas a clear migration of flame toward the leeward side of the mock fuselage is captured. These two-dimensional temperature and flame envelop compare well to the experimentally reported gas phase temperature shadings found in Figs. 4.35 and 4.32 that were provided in the complete report of Suo-Antilla and Gritzo [56].

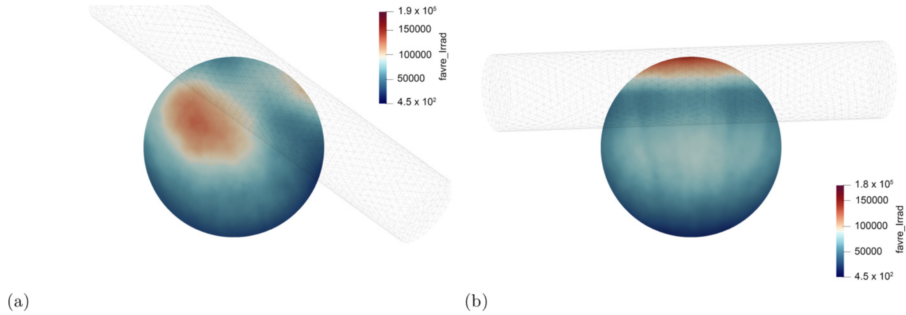

FIG. 23. Surface shadings of time-mean incident radiative flux (R2 pool mesh) at the pool surface for the 2 m/s (a) and 9.5 m/s (b) configurations. The perspective is a user looking downward toward the pool surface, through a low-opacity wire-framed fuselage surface mesh representation. In this set of images, the R0 surface mesh is shown to support unhindered viewing past the fuselage wire-framed surface. The drastic effect of a yawed fuselage drives the formation of substantial asymmetries in heat flux for the 2 m/s configuration.

supports intermittent frontal flame attachment, and crosswind-generated wake, which supports high heating loads within the windward region. The migrated and nonsymmetric flame shape over the lower crosswind configuration is also apparent in Fig. 20.

For an investigation of the time-mean incident radiative flux at the pool surface (perspective is from the top of the domain, looking down) for the most refined mesh (R2), see Fig. 23. For the low-crosswind configuration, an asymmetric heat flux is predicted (bias toward the upwind, spanwise left side), where peak incoming radiative fluxes are located. There is also evidence of an increased pool surface flux at the upper right corner of the pool, indicative of enhanced van Kármán shedding structures. However, as the flame is advected down the cylindrical upper surface due to axial vortical structures, increased incoming radiative heat fluxes are predicted. For the 9.5 m/s configuration, incoming radiative flux shadings concentrate on the far leeward side of the pool where a near symmetric field is predicted with only a slight bias in the counter clockwise direction—again showcasing the minor asymmetry drive by the modest yaw. Interestingly, the peak mean radiative heat fluxes are higher and encompass a larger part of the pool for the 2 m/s configuration.

For a quantitative prediction of maximum and instantaneous heat flux (convective and irradiation), see Table I. Results demonstrate a good comparison to the experimentally provided range of irradiation for the low and high-crosswind configurations. Mean convective heat fluxes at the most refined mesh for low- and high-crosswind configurations are approximately 10% and 5% of the overall heat loading, respectively, suggesting convective heat transfer was likely less resolved in the high-crosswind configuration. For the high-crosswind case, predicted heat fluxes (both irradiation

TABLE I. Maximum Favre-averaged ($.^F$) and instantaneous ($.^I$) heat flux (convective, Q and irradiation, H) for the low- and high-crosswind fire configurations (R0, R1, and R2). Experimentally reported maximum instantaneous H^I are given in parentheses.

		Refinement level		
Crosswind	QoI (kW/m^2)	R0	R1	R2
Low	Q^F/Q^I	23.3/30.0	38.8/24.6	25.1/65.3
Low	H^F/H^I	184.7/344.4	202.3/370.6	218.1/322.4 (220)
High	Q^F/Q^I	4.8/31.2	10.4/52.5	14.4/56.3
High	H^F/H^I	200.9/319.2	216.0/342.9	268.1/374.8 (220–320)

and convective) predominately increase as mesh spacing is reduced, however, the experimentally reported range of irradiation (220–320 $\mathrm{kW/m^2}$) is well predicted. For the low-crosswind use case, a similar trend is found that as the mesh is refined, heat fluxes also increase. Moreover, peak instantaneous irradiation for both the low- and high-crosswind configurations are relatively similar. This finding showcases the complexity associated with wind-driven/bluff-body fire interactions. Specifically, as described in Refs. [8,9], fine-scale mixing increases combustion efficiency and scales with crosswind magnitude. At high crosswinds, this mixing behavior is very difficult to resolve and thus provides motivation for both increased computational speed and efficiency (e.g., GPU porting) and increased model fidelity to circumvent the brute force approach for resolving these features. The mean fire results presented in this study are qualitatively similar to those recently reported in Ref. [14] where a static-coefficient one-equation k_{sgs} approach with local velocity sampling for the equilibrium wall model was used. However, instantaneous irradiation and convective loads were higher with the latest dynamic and exchange-based model suite.

Finally, Suo-Anttila and Gritzo [3] reported skin temperature temperature regions of 1400 K primarily on the windward surface of the mock fuselage (1229–1380 K predicted) for the 2 m/s case, and a 1395 K windswept region under the fuselage at the leeward surface (1290–1306 K predicted) for the 9.5 m/s case. The authors of the experiment also reported intermittent high temperature regions on the windward impingement section of the fuselage, a finding consistent with both our reference skin temperature predictions and the fire dynamics captured in Fig. 18.

V. CONCLUSIONS

WMLES has been deployed to a set of complex bluff-body interaction cases that included an isothermal flow past an elevated cylinder ($G/D = 0.25$) and a large-scale, fire-engulfed mock fuselage. This targeted validation hierarchy was designed for an elevated cylinder in crossflow configuration set that spanned the subcritical and supercritical drag regimes. Results for the isothermal validation study showcased increased predictivity and mesh convergence for QoIs such as drag and pressure coefficient when using a dynamic coefficient procedure for both the algebraic Smagorinsky and transport-based k_{sgs} models. The usage of a fixed exchange location for the equilibrium-based wall model provided a constant sampled y^+ as a function of mesh refinement level at the cylinder surface. The drag crisis phenomenon was well predicted between the subcritical and supercritical regimes, while noting the possible inappropriate usage of a turbulent wall model in laminar regions of the flow. Reduced accuracy for the lift and pressure coefficient predictions at the upper and lower cylindrical sections suggests that this use case can serve as an important validation case study for which future WMLES advances are implemented. However, the overall conclusion was that a nondynamic coefficient turbulence modeling paradigm was not able to adequately predict important QoIs and, perhaps more importantly, did not showcase adequate independence of QoIs with respect to mesh refinement. While the dynamic coefficient paradigm contributed to increased predictively and mesh independence, only when the dynamic procedure was combined with exchange-based velocity sampling (using the "fixed-in-space while refined" procedure) was both predictivity and mesh independence established in drag, lift, and pressure coefficients.

The fire validation case presented used the best practices found in the isothermal validation case where the dynamic coefficient, one-equation k_{sgs} approach was followed—again activating an exchange-based velocity sampling WMLES model suite at all solid surfaces. This multiphysics coupling fire case exercised a low (2.0 m/s) and high (9.5 m/s) mean crosswind profile for an elevated mock fuselage engulfed in an $\mathcal{O}(10)$ m JP-8 pool fire. The fire predictions that were presented accurately captured both the windward-to-leeward transition of flame attachment to the experimental fuselage and the increased heat flux trend as crosswind magnitude was increased. The effect of pool fire dynamics due to an increasing crosswind configuration were outlined, in addition to novel wake vortices and column vortex structures that meandered in and about the flame region.

Our overall conclusions are that a multiphysics, low-Mach WMLES approach can accurately predict both complex fire phenomena and realistic heat flux and temperature ranges required for high-consequence fire safety analysis. As with previous studies, we note that predicted heat fluxes generally increase as mesh resolution increases—especially for high-crosswind configurations. Our findings suggest that other math model-form sensitivities should be explored in the future—including, as was described in Sec. IV B, an equation-based scalar variance and, due to higher-than-expected peak temperatures, both soot model and surrogate fuel evaluation. Finally, with new GPU porting advances conducted within the flag ship Fuego fire code, efforts toward running more refined fire simulations will be pursued as will dynamic pool fire advancement using novel volume-of-fluid unstructured formulations [68].

ACKNOWLEDGMENTS

Sandia National Laboratories is a multi-mission laboratory managed and operated by National Technology & Engineering Solutions of Sandia, LLC (NTESS), a wholly owned subsidiary of Honeywell International Inc., for the U.S. Department of Energy's National Nuclear Security Administration (DOE/NNSA) under Contract No. DE-NA0003525. This written work is authored by an employee of NTESS. The employee, not NTESS, is responsible for its contents. Any subjective views or opinions that might be expressed in the written work do not necessarily represent the views of the U.S. Government. The publisher acknowledges that the U.S. Government retains a nonexclusive, paid-up, irrevocable, world-wide license to publish or reproduce the published form of this written work or allow others to do so, for U.S. Government purposes. The DOE will provide public access to results of federally sponsored research in accordance with the DOE Public Access Plan. Funding for this work was provided by the Advanced Simulations and Computing (ASC) program of Sandia National Laboratories. The lead-author would like to thank Stanford's Center for Turbulence Research Summer Program organizers and participants for many lively and informative technical discussions. Dr. Matt Barone (Sandia National Laboratories) is acknowledged for ongoing WMLES discussions that are driven by synergistic ASC objectives across the low-Mach and reentry application space.

DATA AVAILABILITY

The data supporting this study's findings are available within the article.

APPENDIX A: COMPREHENSIVE ELEVATED CYLINDER QOIS

Appendix A contains the pressure coefficient, lift coefficient, wall shear stress, instantaneous velocity renderings, and Q criterion renderings for each combination of turbulence model, wall model, and flow condition, for the isothermal case which were not previously presented in the body of the paper.

1. Complete C_p overview

Figures 24 and 25 show the C_p profiles for the local wall modeling methodology (the exchange method was presented in Sec. III C) for each turbulence model. The local velocity sampling wall modeling procedure has similar mesh convergence and predictivity as the exchange-based approach. The only outlier is the R2 dynamic models for the subcritical flow. Here we note a slightly nonsymmetric shape of the C_p curve, depending on the turbulence model, and find that the upper (roughly 90°) and lower (roughly 270°) stations predicted substantially lower local pressure coefficient values as compared to the coarse experimental values.

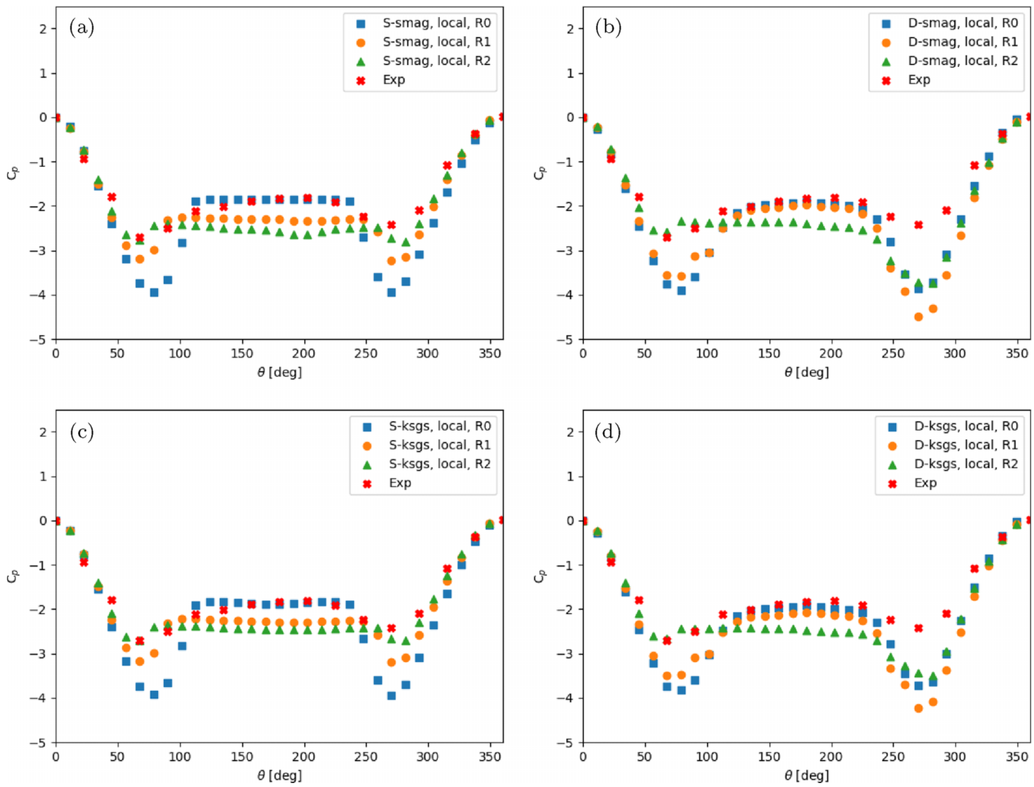

FIG. 24. C_p for the subcritical regime as a function of angle, including both the static and dynamic Smagorinsky model suite (a) and (b) as compared to the static and dynamic k_{sgs} model (c) and (d), shown with experimental results from Ref. [29]. All simulation results showcase local velocity sampling.

2. Complete C_L overview

Tables II and III along with Figs. 26–29, present the C_L for all permutations of turbulence model, flow, and wall model. Based on extraction of the time-mean lift condition from Yang *et al.* [29], the low- and high-Reynolds number are 0.268 and 0.279. While the exchange wall model diminishes

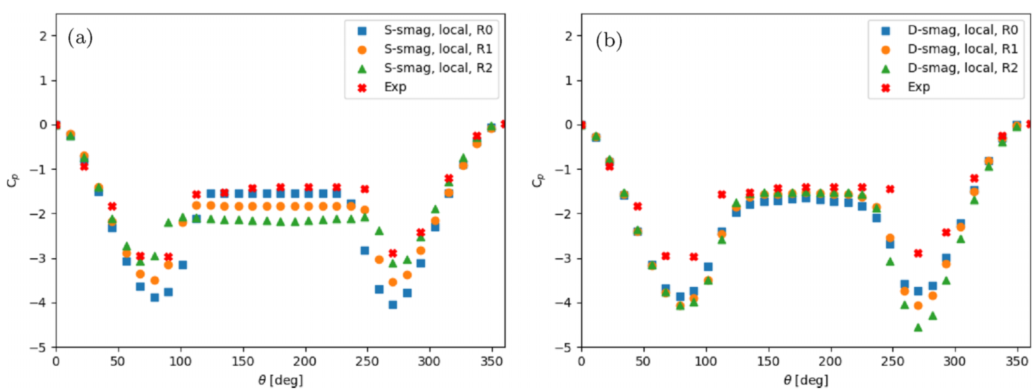

FIG. 25. C_p for the supercritical regime as a function of angle for the static and dynamic Smagorinsky model suite (a) and (b), shown with experimental results from Ref. [29]. All simulation results showcase local velocity sampling.

TABLE II. Subcritical average C_L for all turbulence models [Smagorinsky (smag) and k_{sgs} (ksgs) with both the static (S-) and dynamic (D-) formulation] using exchange-based and local velocity sampling (R0, R1, and R2 mesh refinements shown).

		Refinement level		
Turbulence model	Wall model	R0	R1	R2
S-smag	Local	0.048	0.083	0.147
S-smag	Exchange	0.076	−0.075	−0.129
D-smag	Local	0.156	−0.224	−0.405
D-smag	Exchange	0.044	0.004	0.049
S-ksgs	Local	0.080	0.100	0.147
S-ksgs	Exchange	0.139	−0.061	−0.134
D-ksgs	Local	0.191	−0.171	−0.290
D-ksgs	Exchange	0.194	−0.001	0.004

the differences between mesh resolutions, overall the lift coefficient is only moderately predicted for some model-forms. Reconciling the lift predictions with the pressure coefficient results suggests that the WMLES approach, in absence of a transition model, does not precisely predict boundary layer attachment, transition, and separation. At the upper and lower cylinder stations, C_p prediction is in error and drastically affects the quality of the lift prediction. More work regarding advanced wall modeling approaches are needed, noting that this case serves as an exceptional exemplar to evaluate all WMLES approaches in the low-Mach regime.

3. Complete wall shear stress, τ_w, overview

Figures 30–33 presents the wall shear stress for all permutations of turbulence model, flow, and wall model. Here we can see strong convergence with the exchange based wall model for turbulence models and flow conditions, while the local wall model shows weaker mesh convergence. We also note that the dynamic procedure displays better mesh convergence than the static, however the difference pales in comparison to the differences seen due to the wall model.

4. Complete velocity and shear stress shadings overview

Figures 34–39 presents the renderings for the velocity on vertical plane and wall shear stress on the cylinder and ground surface for all permutations of turbulence model, flow, and wall model (with the exception of the dynamic k_{sgs} with exchange wall modeling, which is presented in Sec.

TABLE III. Supercritical averaged C_L for all turbulence models [Smagorinsky (smag) and k_{sgs} (ksgs) with both the static (S-) and dynamic (D-) formulation] using exchange-based and local velocity sampling (R0, R1, and R2 mesh refinements shown).

		Refinement level		
Turbulence model	Wall model	R0	R1	R2
S-smag	Local	0.063	0.070	0.068
S-smag	Exchange	0.069	0.020	−0.081
D-smag	Local	0.189	0.232	−0.008
D-smag	Exchange	0.045	0.118	0.172
D-ksgs	Exchange	0.236	0.156	0.212

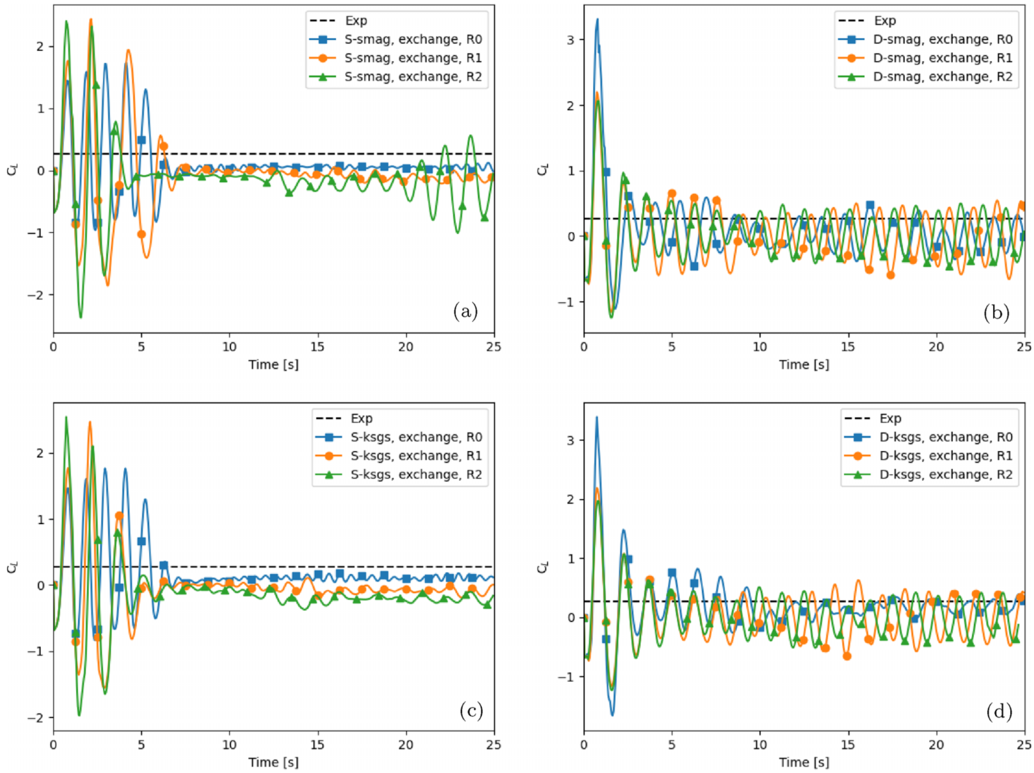

FIG. 26. Subcritical C_L as a function of time, including both the static and dynamic Smagorinsky model suite (a) and (b) as compared to the static and dynamic k_{sgs} model (c) and (d). All simulation results showcase the exchange-based velocity sampling. The average experimental value from Ref. [29] is also shown.

III A). With the exchange based wall model, we see higher wall shear stresses on the cylinder and ground, while the dynamic models tend to show more defined vortex shedding.

5. Q Criterion

Figures 40–45 presents the volume renderings for the Q criterion and wall shear stress on the cylinder and ground surface for all permutations of turbulence model, flow, and wall model (with the exception of the dynamic k_{sgs} with exchange wall modeling, which is presented in Sec. III A). The dynamic approaches tend to capture large-scale vortical structures on the leeward side of the cylinder more clearly. For boundary layer transition based on the steady inflow specification, the k_{sgs} turbulence models (both static and dynamic) tend toward a fast transition near the inlet. The Smagorinsky supercritical configurations frequently showcase a delayed turbulent transition that is a function of the static/dynamic and local/exchange modeling choices.

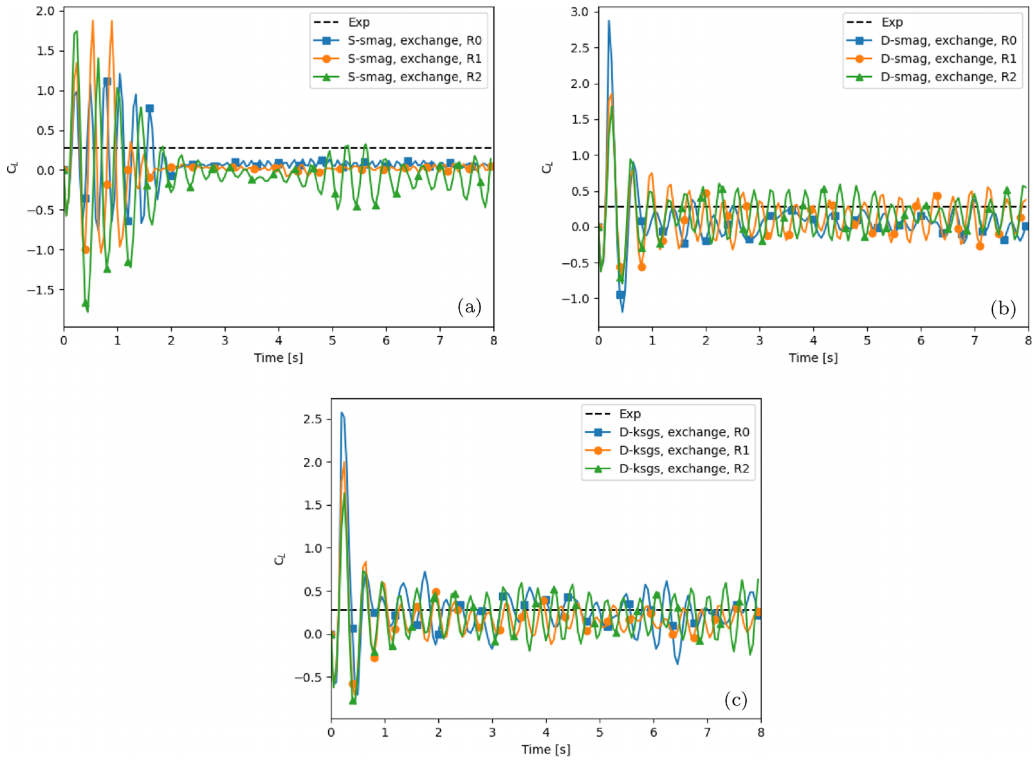

FIG. 27. Supercritical C_L as a function of time, including both the static and dynamic Smagorinsky model suite (a) and (b) as compared to the dynamic k_{sgs} model (c). All simulation results showcase the exchange-based velocity sampling. The average experimental value from Ref. [29] is also shown.

APPENDIX B: FIRE DYNAMICS MESH REFINEMENT OVERVIEW

The effect of mesh refinement on representative fire structures are shown in Figs. 46 and 47, respectively. As with previous findings outlined in Refs. [7–9], the effect of refinement has a pronounced effect on resolved flame structure, while noting that all simulation results nominally predict either predominant windward (2 m/s) or leeward (9.5 m/s) flame attachment trend. All mesh resolutions showcase the desired migration of flame shape from the windward to leeward fuselage, while noting that the coarse mesh might be best applied to a RANS-based methodology. Efforts to provide a third refined mesh (R3) are underway.

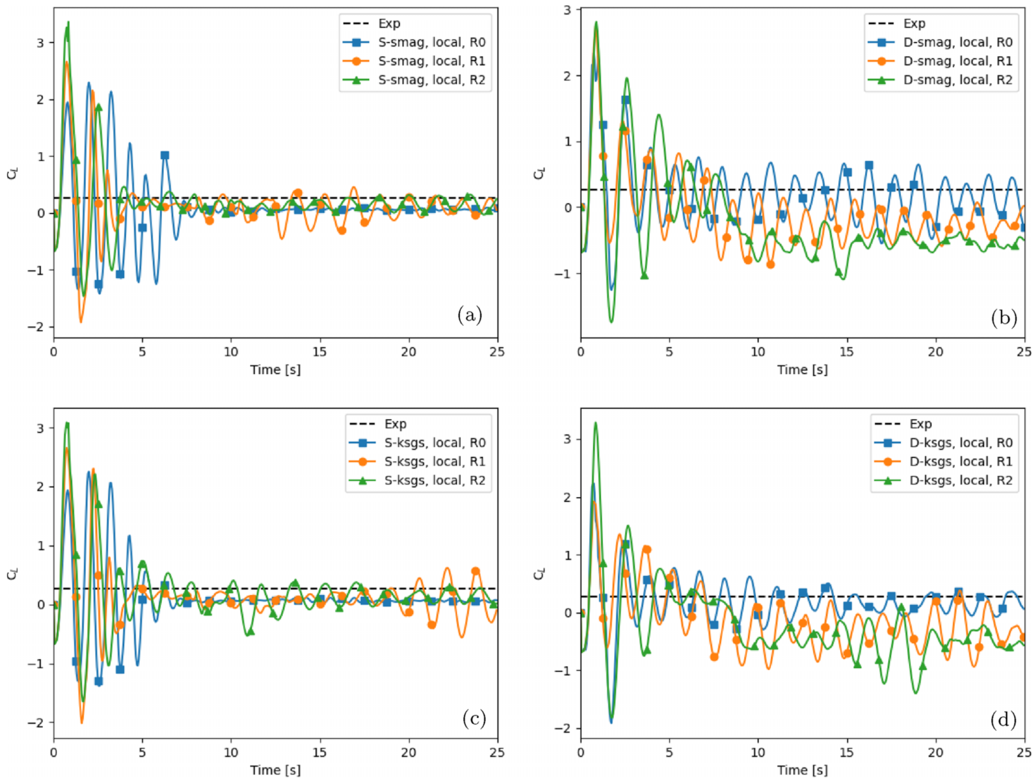

FIG. 28. Subcritical C_L as a function of time, including both the static and dynamic Smagorinsky model suite (a) and (b) as compared to the static and dynamic k_{sgs} model (c) and (d). All simulation results showcase local velocity sampling. The average experimental value from Ref. [29] is also shown.

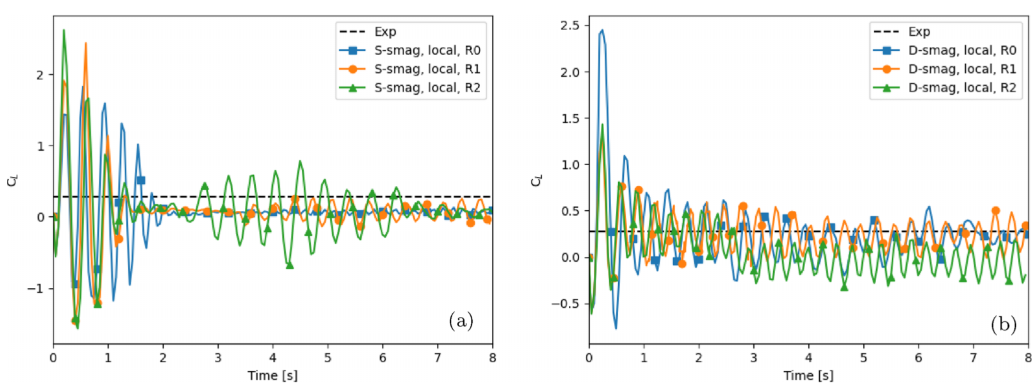

FIG. 29. Supercritical C_L as a function of time for the static (a) and dynamic (b) Smagorinsky model suite using local velocity sampling. The average experimental value from Ref. [29] is also shown.

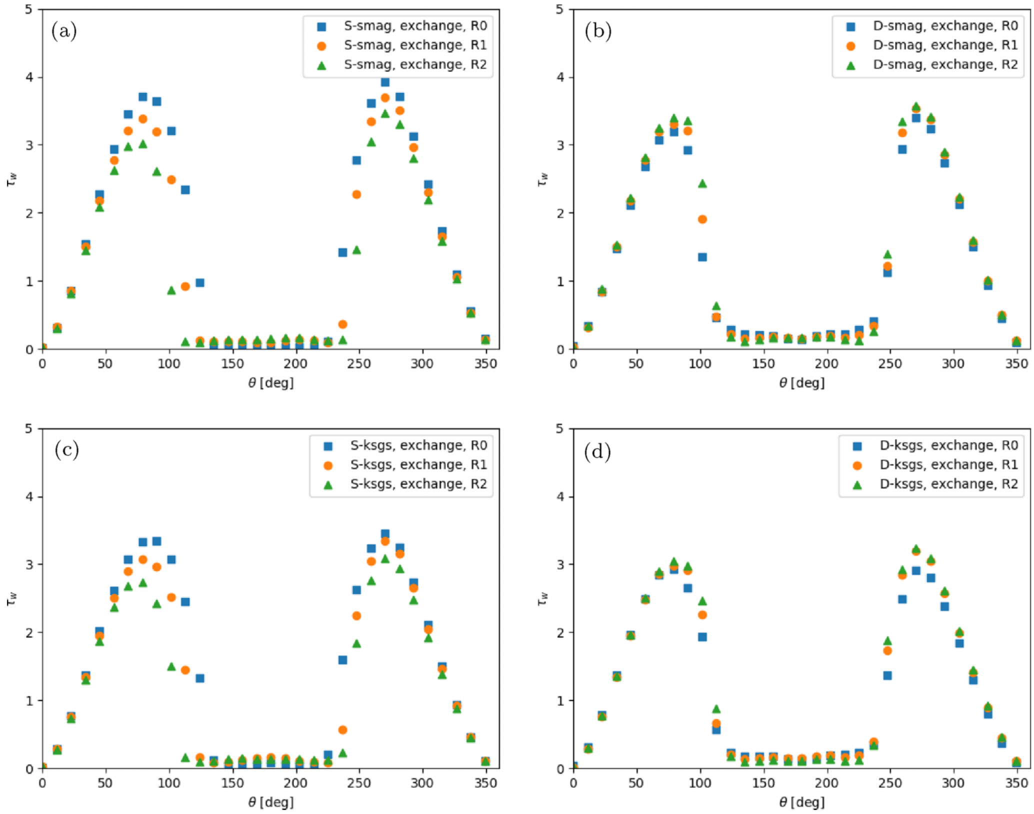

FIG. 30. Subcritical τ_w as a function of angle, including both the static and dynamic Smagorinsky model suite (a) and (b) as compared to the static and dynamic k_{sgs} model (c) and (d). All simulation results showcase exchange-based velocity sampling.

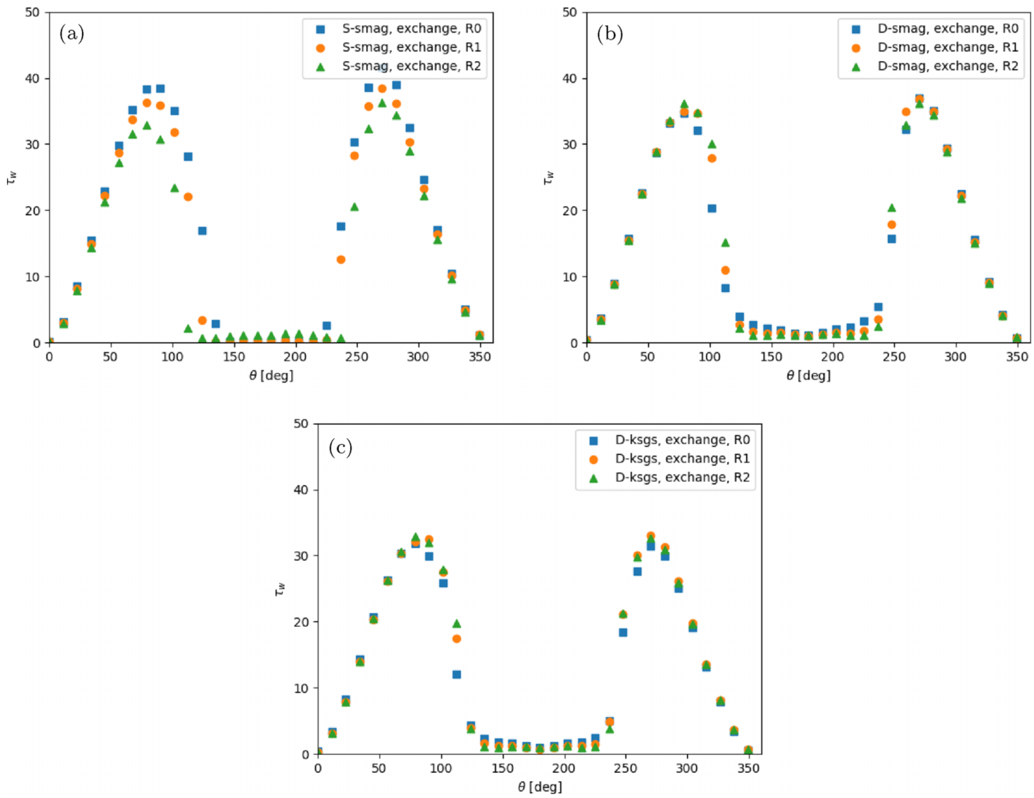

FIG. 31. Supercritical τ_w as a function of angle, including both the static and dynamic Smagorinsky model suite (a) and (b) as compared to the dynamic k_{sgs} model (c). All simulation results showcase the exchange-based velocity sampling.

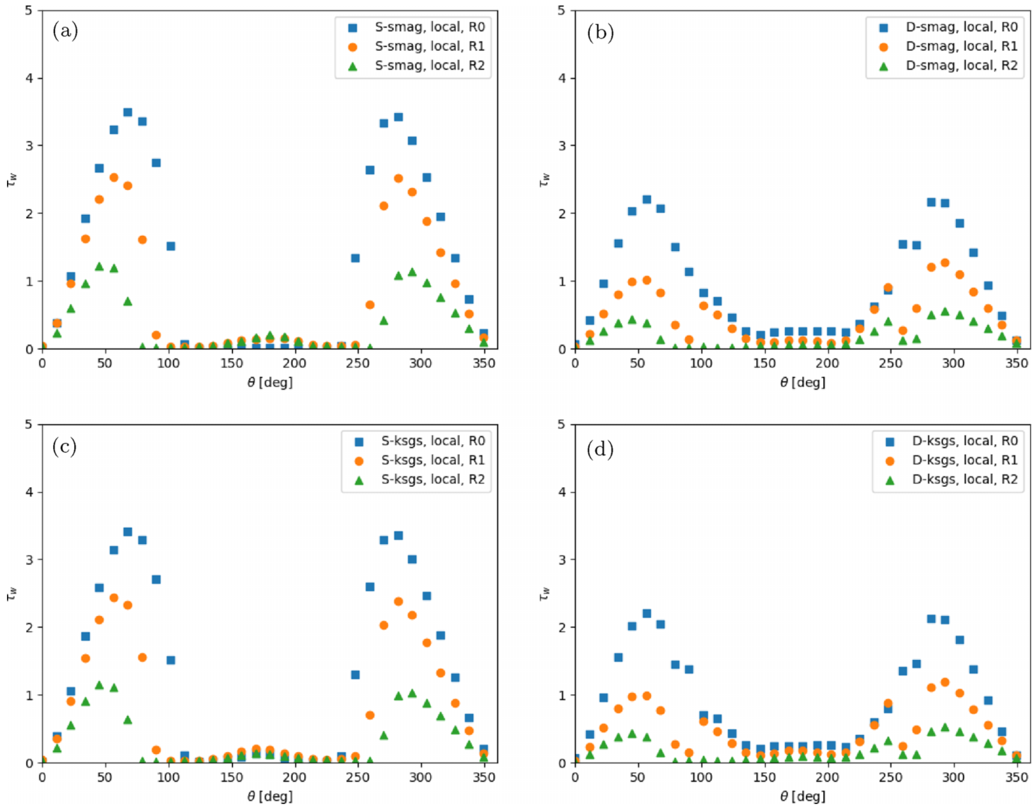

FIG. 32. Subcritical τ_w as a function of angle, including both the static and dynamic Smagorinsky model suite (a) and (b) as compared to the static and dynamic k_{sgs} model (c) and (d). All simulation results showcase local velocity sampling.

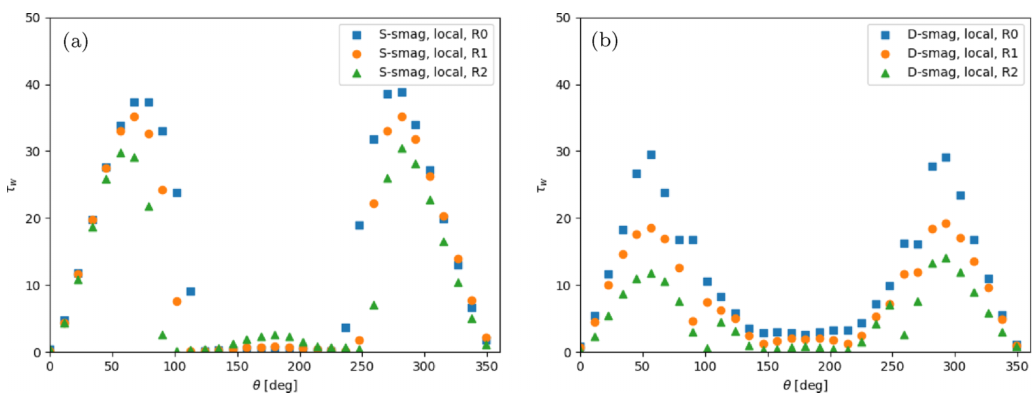

FIG. 33. Supercritical τ_w as a function of angle for the static (a) and dynamic (b) Smagorinsky model suite using local velocity sampling.

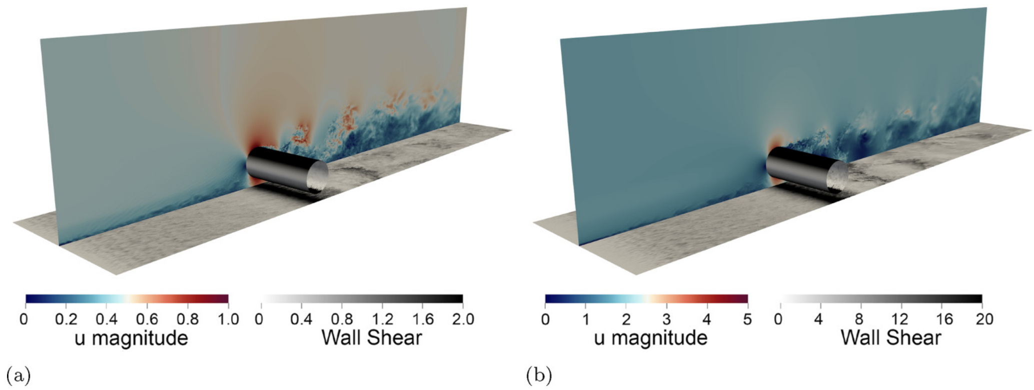

FIG. 34. Velocity magnitude (vertical plane) and wall shear stress (cylinder and ground surface) shadings for the subcritical (a) and supercritical (b) configurations. The model suite depicted activated the dynamic Smagorinsky with exchange-based velocity sampling.

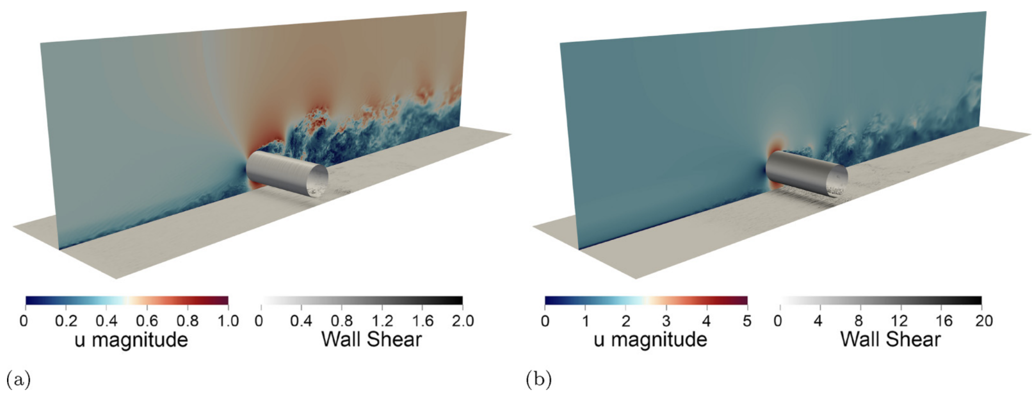

FIG. 35. Velocity magnitude (vertical plane) and wall shear stress (cylinder and ground surface) shadings for the subcritical (a) and supercritical (b) configurations. The model suite depicted activated the dynamic Smagorinsky with local velocity sampling.

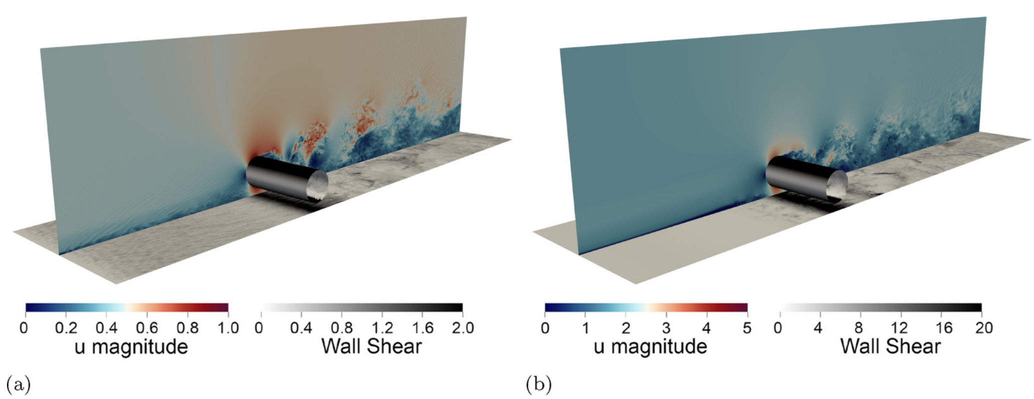

FIG. 36. Velocity magnitude (vertical plane) and wall shear stress (cylinder and ground surface) shadings for the subcritical (a) and supercritical (b) configurations. The model suite depicted activated the static Smagorinsky with exchange-based velocity sampling.

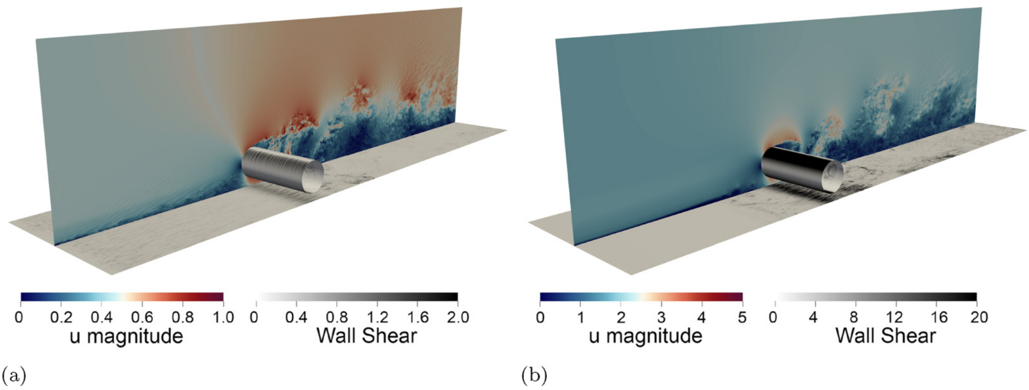

FIG. 37. Velocity magnitude (vertical plane) and wall shear stress (cylinder and ground surface) shadings for the subcritical (a) and supercritical (b) configurations. The model suite depicted activated the static Smagorinsky with local velocity sampling.

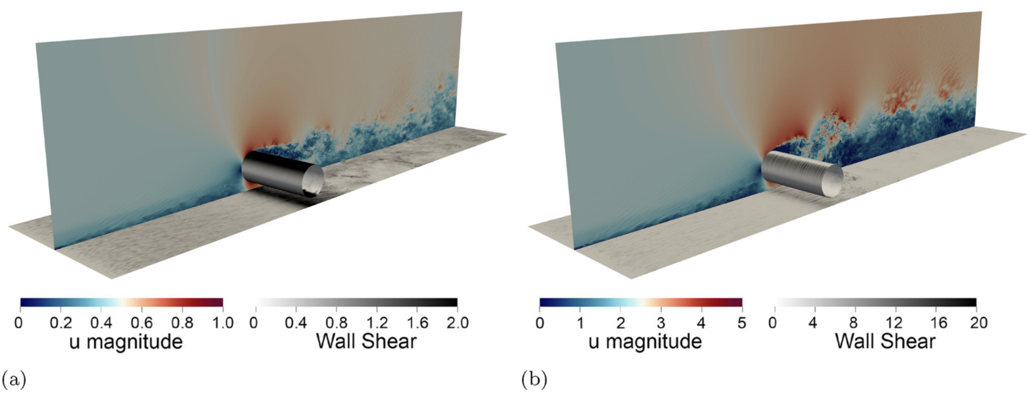

FIG. 38. Velocity magnitude (vertical plane) and wall shear stress (cylinder and ground surface) shadings for the subcritical configuration. The model suite depicted activated the static k_{sgs} with exchange-based (a) and local (b) velocity sampling.

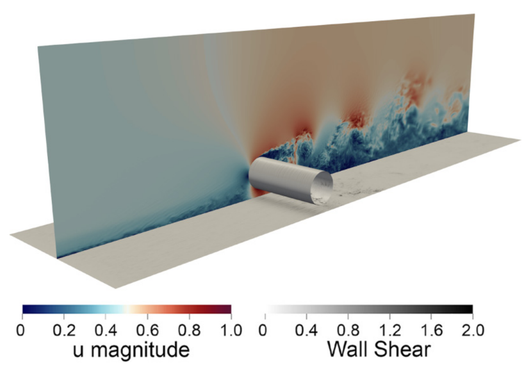

FIG. 39. Velocity magnitude (vertical plane) and wall shear stress (cylinder and ground surface) shadings for the subcritical configuration. The model suite depicted activated the dynamic k_{sgs} with local velocity sampling.

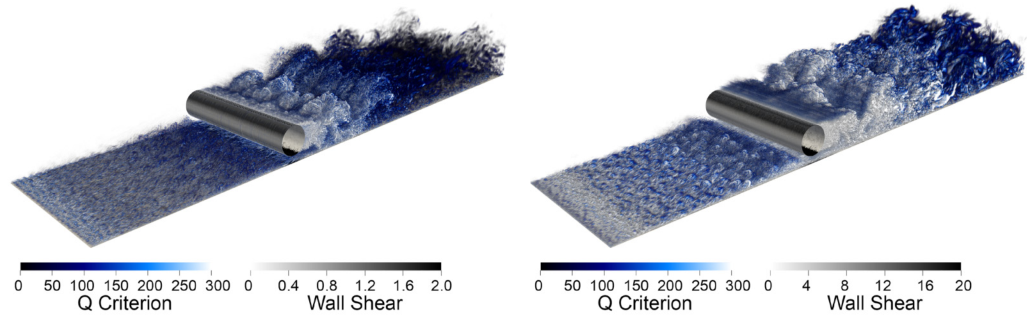

(a) (b)

FIG. 40. Q criterion and wall shear stress (cylinder and ground surface) shadings for the subcritical (a) and supercritical (b) configurations. The model suite depicted activated the dynamic Smagorinsky with exchange-based velocity sampling.

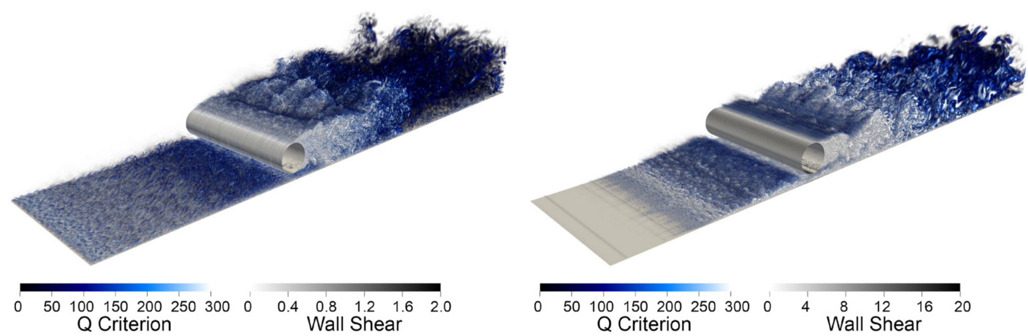

(a) (b)

FIG. 41. Q criterion and wall shear stress (cylinder and ground surface) shadings for the subcritical (a) and supercritical (b) configurations. The model suite depicted activated the dynamic Smagorinsky with local velocity sampling.

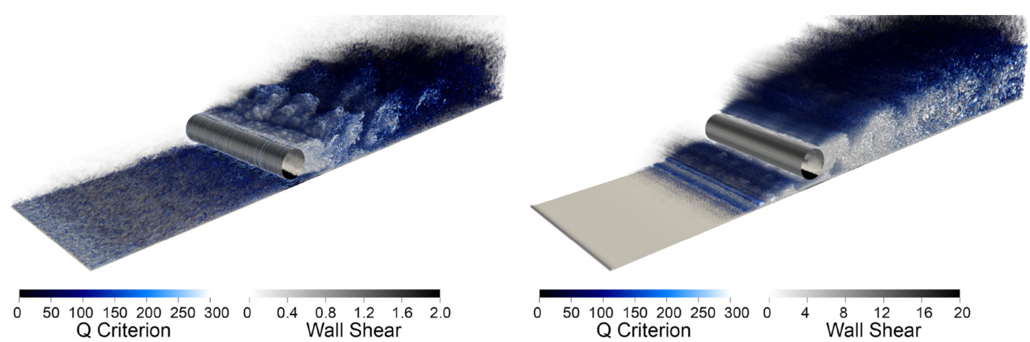

(a) (b)

FIG. 42. Q criterion and wall shear stress (cylinder and ground surface) shadings for the subcritical (a) and supercritical (b) configurations. The model suite depicted activated the static Smagorinsky with exchange-based velocity sampling.

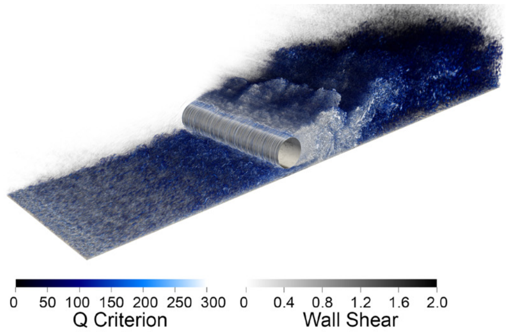

(a)

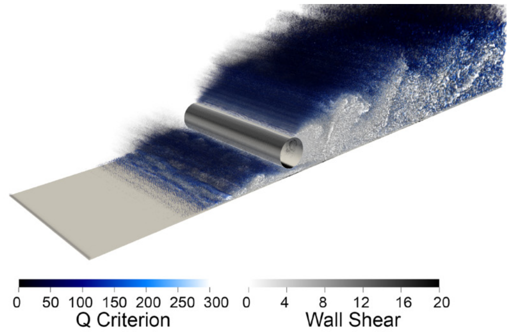

(b)

FIG. 43. Q criterion and wall shear stress (cylinder and ground surface) shadings for the subcritical (a) and supercritical (b) configurations. The model suite depicted activated the static Smagorinsky with local velocity sampling.

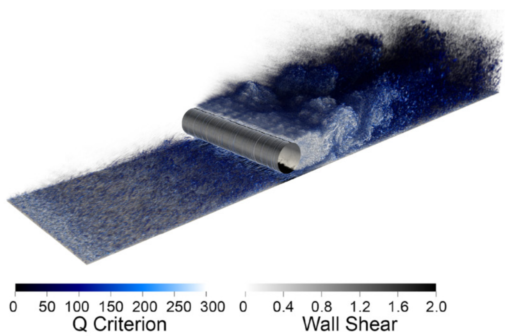

(a)

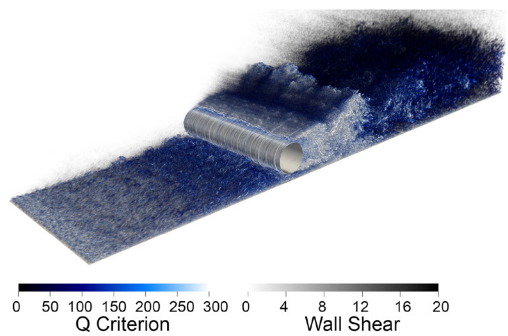

(b)

FIG. 44. Q criterion and wall shear stress (cylinder and ground surface) shadings for the subcritical configuration. The model suite depicted activated the static k_{sgs} with exchange-based (a) and local (b) velocity sampling.

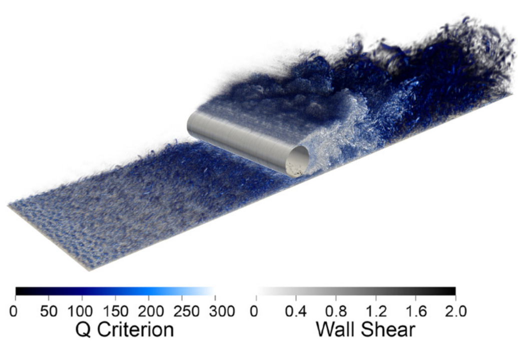

FIG. 45. Q criterion and wall shear stress (cylinder and ground surface) shadings for the subcritical configuration. The model suite depicted activated the dynamic k_{sgs} with local velocity sampling.

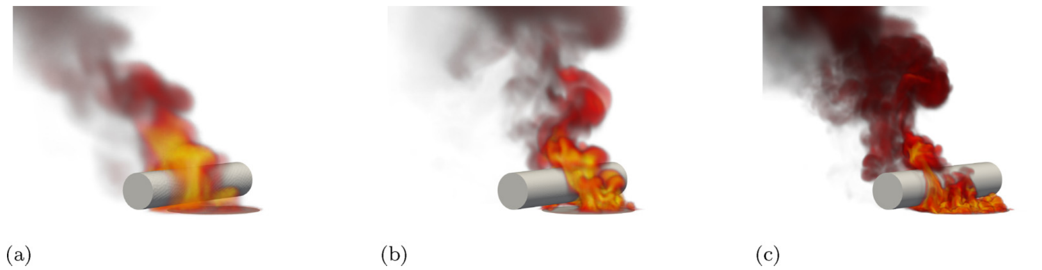

FIG. 46. The effect of uniform refinement on fire structure for the 2.0 m/s configuration; shown are volume-renderings of the gas phase temperature field. Mesh refinement increases from left to right.

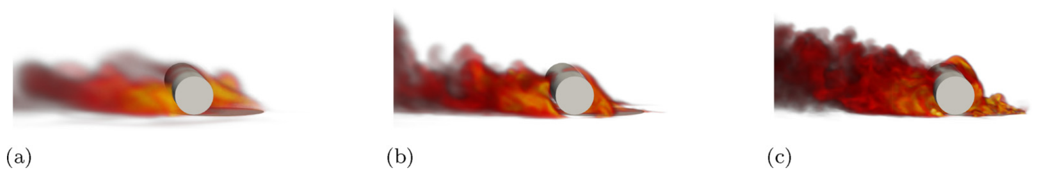

FIG. 47. The effect of uniform refinement on fire structure for the 9.5 m/s configuration; shown are volume-renderings of the gas phase temperature field. Mesh refinement increases from left to right.

[1] C. S. Lam, Thermal characterization of a pool fire in crosswind with a large adjacent cylindrical object: Experimental design, Ph.D. thesis, University of Waterloo, 2003.

[2] S. R. Tieszen, T. J. O'Hern, E. J. Weckman, and R. W. Schefer, Experimental study of the effect of fuel mass flux on a 1-m-diameter methane fire and comparison with a hydrogen fire, Combust. Flame **139**, 126 (2004).

[3] J. Suo-Anttila and L. Gritzo, The effects of wind on fire environments containing large cylinders, Combust. Sci. Technol. **181**, 68 (2008).

[4] A. Luketa and T. Blanchat, The phoenix series large-scale methane gas burner experiments and liquid methane pool fires experiments on water, Combust. Flame **162**, 4497 (2015).

[5] S. Tieszen, S. Domino, and A. Black, Validation of a simple turbulence model suitable for closure of temporally-filtered Navier-Stokes equations using a helium plume, Tech. Rep. No. OSTI ID No. 923079 (U.S. Department of Energy, OSTI, Washington, DC, 2005).

[6] S. Domino, C. Moen, S. Burns, and G. Evans, Sierra/fuego: A multi-mechanics fire environment simulation tool, in *Proceedings of the 41st Aerospace Sciences Meeting and Exhibit* (AIAA, Reston, VA, 2003).

[7] S. P. Domino, J. Hewson, R. Knaus, and M. Hansen, Predicting large-scale pool fire dynamics using an unsteady flamelet- and large-eddy simulation-based model suite, Phys. Fluids **33**, 085109 (2021).

[8] S. N. Scott and S. P. Domino, A computational examination of large-scale pool fires: Variations in crosswind velocity and pool shape, Flow **2**, E32 (2022).

[9] S. P. Domino, On the subject of large-scale pool fires and turbulent boundary layer interactions, Phys. Fluids **36**, 025163 (2024).

[10] S. B. Pope, Ten questions concerning the large-eddy simulation of turbulent flows, New J. Phys. **6**, 35 (2004).

[11] Y. Xin, J. Gore, K. Mcgrattan, R. Rehm, and H. Baum, Large eddy simulation of buoyant turbulent pool fires, Proc. Combust. Inst. **29**, 259 (2002).

[12] M. Jangi, M. Altarawneh, and B. Z. Dlugogorski, Large-eddy simulation of methanol pool fires using an accelerated stochastic fields method, Combust. Flame **173**, 89 (2016).
[13] M. Safarzadeh, G. Heidarinejad, and H. Pasdarshahri, Evaluation of les sub-grid scale models and time discretization schemes for prediction of convection effect in a buoyant pool fire, Heat Mass Transfer **57**, 631 (2021).
[14] S. Domino, Credibility assessment for WMLES that includes fire-engulfed objects in crosswind, in *Studying Turbulence Using Numerical Simulation Databases—XIV*, edited by P. Moin and B. McKeon (Stanford Center for Turbulence Research, Stanford, CA, 2024), pp. 363–372.
[15] M. A. Meehan, J. C. Hewson, and P. E. Hamlington, High resolution numerical simulations of methane pool fires using adaptive mesh refinement, Proc. Combust. Inst. **40**, 105768 (2024).
[16] M. M. Ahmed and A. Trouvé, Large eddy simulation of the unstable flame structure and gas-to-liquid thermal feedback in a medium-scale methanol pool fire, Combust. Flame **225**, 237 (2021).
[17] F. Nmira and J.-L. Consalvi, Local contributions of resolved and subgrid turbulence-radiation interaction in LES/presumed FDF modelling of large-scale methanol pool fires, Int. J. Heat Mass Transf. **190**, 122746 (2022).
[18] A. Luketa, V. Romero, S. Domino, D. Glaze, M. Sherman, and V. Figueroa, Validation and uncertainty quantification of fuego simulations of calorimeter heating in a wind-driven hydrocarbon pool fire, Tech. Rep. No. SAND2009-7605 (Sandia National Laboratories SAND Series, Albuquerque, NM, 2009).
[19] A. Brown, W. Gill, G. Evans, and D. Jarboe, Validation predictions of a 13 m/s cross-wind fire for Fuego and the University of Waterloo dataset, Tech. Rep. No. SAND2008-0919 (Sandia National Laboratories SAND Series, Albuquerque, NM, 2008).
[20] S. Zhang, W. Fang, L. Shi, J. Liu, J. Liu, J. Wang, and B. Cong, Fire plume characteristics of annular pool fire with different cylindrical obstacles in a ship engine room, Ocean Eng. **276**, 114253 (2023).
[21] J. A. Hubbard, S. P. Domino, J. C. Hewson, and F. Pierce, Numerical investigation of mixing and heat transfer in a 7.9 m jp-8 pool fire, Case Stud. Therm. Eng. **60**, 104702 (2024).
[22] H. Wang and G. Da Wang, Interaction between crosswind and aviation-fuel fire engulfing a full-scale composite-type aircraft: A numerical study, Aerospace **2**, 279 (2015).
[23] M. Modest, *Radiative Heat Transfer*, 3rd ed. (Academic Press, Oxford, UK, 2013).
[24] V. Drean, B. Girardin, B. Guillaume, R. Chiva, J. Colombiano, B. Rengel, T. Desmurger, G. Mitanchez, and E. Guillaume, Large scale pool fire with a fully engulfed tank—Experimental data and numerical validation of the flame height and flame behaviour around the tank, J. Loss Prev. Process Ind. **91**, 105360 (2024).
[25] K. McGrattan, R. McDermott, C. Weinschenk, and G. Forney, Fire Dynamics Simulator, Technical Reference Guide, 6th ed., Special Publication (NIST SP), Tech. Rep. No. 1018 (National Institute of Standards and Technology, Gaithersburg, MD, 2013).
[26] J. M. Forthofer and S. L. Goodrick, Review of vortices in wildland fire, J. Combust. **2011**, 984363 (2011).
[27] W. E. Heilman, Atmospheric turbulence and wildland fires: A review, Int. J. Wildland Fire **32**, 476 (2023).
[28] J. Larsson, S. Kawai, J. Bodart, and I. Bermejo-Moreno, Large eddy simulation with modeled wall-stress: Recent progress and future directions, Mech. Eng. Rev. **3**, 15-00418 (2016).
[29] F. Yang, H. An, and L. Cheng, Drag crisis of a circular cylinder near a plane boundary, Ocean Eng. **154**, 133 (2018).
[30] S. T. F. D. Team, SIERRA Low Mach Module: Fuego Theory Manual—Version 5.10, Tech. Rep. No. SAND2022-12438 (Sandia National Laboratories, 2022a).
[31] J. Smagorinsky, General circulation experiments with the primitive equations. I. The basic experiment, Monthly Weather Rev. **91**, 99 (1963).
[32] A. Yoshizawa, Bridging between eddy-viscosity-type and second-order turbulence models through a two-scale turbulence theory, Phys. Rev. E **48**, 273 (1993).
[33] M. Germano, U. Piomelli, P. Moin, and W. H. Cabot, A dynamic subgrid-scale eddy viscosity model, Phys. Fluids A Fluid Dyn. **3**, 1760 (1991).
[34] W.-W. Kim, S. Menon, W.-W. Kim, and S. Menon, Application of the localized dynamic subgrid-scale model to turbulent wall-bounded flows, in Proceedings of the 35th Aerospace Sciences Meeting and

Exhibit, Aerospace Sciences Meetings (American Institute of Aeronautics and Astronautics, Reston, VA, 1997).

[35] S. Domino, Sierra low Mach Module Nalu: Theory Manual, Tech. Rep. No. SAND2015-3107W (Sandia National Laboratories SAND Series, Albuquerque, NM, 2015), https://nalu.readthedocs.io/en/latest/source/theory/index.html (last accessed April, 2025).

[36] S. Domino, Toward verification of formal time accuracy for a family of approximate projection methods using the method of manufactured solutions, in *Studying Turbulence Using Numerical Simulation Databases—XI*, edited by P. Moin and N. Mansour (Stanford Center for Turbulence Research, Stanford, CA, 2006), pp. 163–177.

[37] S. P. Domino, Design-order, nonconformal low-Mach fluid algorithms using a hybrid CVFEM/DG approach, J. Comput. Phys. **359**, 331 (2018).

[38] S. P. Domino, P. Sakievich, and M. Barone, An assessment of atypical mesh topologies for low-Mach large-eddy simulation, Comput. Fluids **179**, 655 (2019).

[39] S. Domino, Unstructured finite volume approaches for turbulence, in *Numerical Methods in Turbulence Simulation*, edited by R. D. Moser (Academic Press, an imprint of Elsevier, London, UK; San Diego, CA, 2023), Chap. 7, pp. 285–317.

[40] C. L. V. Jayatilleke, The influence of Prandtl number and surface roughness on the resistance of the laminar sublayer to momentum and heat transfer, Prog. Heat Mass Transfer **1**, 193 (1969).

[41] H. M. Blackburn and W. H. Melbourne, The effect of free-stream turbulence on sectional lift forces on a circular cylinder, J. Fluid Mech. **306**, 267 (1996).

[42] N. Peters, *Turbulent Combustion* (IOP Publishing, Cambridge, UK, 2001).

[43] I. Aksit and J. Moss, A hybrid scalar model for sooting turbulent flames, Combust. Flame **145**, 231 (2006).

[44] C. Thurgood, A. Pollard, and A. Becker, The TN quadrature set for the discrete ordinates method, J. Heat Transf. **117**, 1068 (1995).

[45] S. T. F. D. Team, SIERRA Multimechanics Module: Aria User Manual—Version 5.10, Tech. Rep. No. SAND2022-12436 (Sandia National Laboratories, 2022b).

[46] S. Domino, G. Wagner, A. Luketa-Hanlin, A. Black, and J. Sutherland, Verification for multi-mechanics applications, in Proceedings of the 48th AIAA/ASME/ASCE/AHS/ASC Structures, Structural Dynamics, and Materials Conference, Structures, Structural Dynamics, and Materials and Co-located Conferences (American Institute of Aeronautics and Astronautics, Reston, VA, 2007).

[47] M. Van Dyke, *An Album of Fluid Motion* (The Parabolic Press, Stanford, CA, 1982).

[48] P. Catalano, M. Wang, G. Iaccarino, and P. Moin, Numerical simulation of the flow around a circular cylinder at high Reynolds numbers, Int. J. Heat Fluid Flow **24**, 463 (2003), selected papers from the *Fifth International Conference on Engineering Turbulence Modelling and Measurements*.

[49] O. Lehmkuhl, I. Rodríguez, R. Borrell, J. Chiva, and A. Oliva, Unsteady forces on a circular cylinder at critical Reynolds numbers, Phys. Fluids **26**, 125110 (2014).

[50] G. S. West and C. J. Apelt, The effects of tunnel blockage and aspect ratio on the mean flow past a circular cylinder with Reynolds numbers between 104 and 105, J. Fluid Mech. **114**, 361 (1982).

[51] P. W. Bearman and M. M. Zdravkovich, Flow around a circular cylinder near a plane boundary, J. Fluid Mech. **89**, 33 (1978).

[52] NOAA, Comparative climate data for the United States through 2018, Tech. Rep. No. CCD-2018 (National Oceanic and Atmospheric Administration, Washington DC, 2018).

[53] J. Hunt, A. Wray, and P. Moin, Eddies, streams, and convergence zones in turbulent flows, in *Studying Turbulence Using Numerical Simulation Databases—II*, edited by P. Moin, W. Reynolds, and J. Kim (Stanford Center for Turbulence Research, Stanford, CA, 1988), pp. 193–208.

[54] E. T. Dauricio and J. L. F. Azevedo, A wall model for external laminar boundary layer flows applied to the wall-modeled LES framework, J. Comput. Phys. **484**, 112087 (2023).

[55] M. Heroux, R. Bartlett, V. Howle, R. Hoekstra, J. Hu, T. Kolda, R. Lehoucq, K. Long, R. Pawlowski, E. Phipps, A. Salinger, J. Thornquist, R. Tuminaro, J. Willenbring, and A. Williams, An overview of Trilinos, Tech. Rep. No. SAND-20032927 (Sandia National Laboratories, Albuquerque, NM, 2003).

[56] J. Suo-Antilla and L. Gritzo, Thermal measurements from a series of tests with a large cylindrical calorimeter on the leeward edge of a JP-8 pool fire in crossflow, Tech. Rep. No. SAND-20011986 (Sandia National Laboratories, Albuquerque, NM, 2001).

[57] M. Matsumoto, T. Yagi, Y. Shigemura, and D. Tsushima, Vortex-induced cable vibration of cable-stayed bridges at high reduced wind velocity, J. Wind Eng. Ind. Aerodyn. **89**, 633 (2001), 10th International Conference on Wind Engineering.

[58] M. Matsumoto, Y. Daito, T. Kanamura, Y. Shigemura, S. Sakuma, and H. Ishizaki, Wind-induced vibration of cables of cable-stayed bridges, J. Wind Eng. Ind. Aerodyn. **74-76**, 1015 (1998).

[59] S. Cheng, G. L. Larose, M. G. Savage, H. Tanaka, and P. A. Irwin, Experimental study on the wind-induced vibration of a dry inclined cable—Part I: Phenomena, J. Wind Eng. Ind. Aerodyn. **96**, 2231 (2008).

[60] E. Knudsen, E. S. Richardson, E. M. Doran, H. Pitsch, and J. H. Chen, Modeling scalar dissipation and scalar variance in large eddy simulation: Algebraic and transport equation closures, Phys. Fluids **24**, 055103 (2012).

[61] T. Cetegen, B. Ahmed, Experiments on the periodic instability of buoyant plumes and pool fires, Combust. Flame **93**, 157 (1993).

[62] S. Tieszen, On the fluids mechanics of fires, Annu. Rev. Fluid Mech. **33**, 67 (2001).

[63] T. O'Hern, E. Weckman, A. Gerhart, S. Tiezen, and R. Sheffer, Experimental study of a turbulent buoyant helium plume, J. Fluid Mech. **544**, 143 (2005).

[64] K. Mahesh, The interaction of jets with crossflow, Annu. Rev. Fluid Mech. **45**, 379 (2013).

[65] See Supplemental Material at http://link.aps.org/supplemental/10.1103/PhysRevFluids.10.054604 for a volume-rendered temperature movie.

[66] S. Tieszen, V. Nicolette, L. Gritzo, J. Holen, D. Murray, and J. Moya, Vortical structures in pool fires: Observation, speculation, and simulation, Tech. Rep. No. SAND96-2607 (Sandia National Laboratories SAND Series, Albuquerque, NM, 1996).

[67] T. F. Fric and A. Roshko, Vortical structure in the wake of a transverse jet, J. Fluid Mech. **279**, 1 (1994).

[68] T. Rodgers, S. Domino, M. Grillet, A. McMaster, and M. Heiden, Increasing CO_2 capture rate in liquid-solvent direct-air carbon capture via additive manufacturing, Tech. Rep. No. SAND2023-13411R (Sandia National Laboratories, Albuquerque, NM, 2023).